2018

Analyzing the Spectral Energy Cascade in Turbulent Channel Flow

João Rodrigo Andrade

Ramon Silva Martins

Gilmar Mompean

Laurent Thais

Thomas B. Gatski
Old Dominion University, gatski@ccpo.odu.edu

Original Publication Citation

Andrade, J. R., Martins, R. S., Mompean, G., Thais, L., & Gatski, T. B. (2018). Analyzing the spectral energy cascade in turbulent channel flow. *Physics of Fluids, 30(*6), 065110. doi:10.1063/1.5022653

Analyzing the spectral energy cascade in turbulent channel flow

João Rodrigo Andrade,[1,2,a)] Ramon Silva Martins,[1,3,b)] Gilmar Mompean,[1,c)] Laurent Thais,[1,d)] and Thomas B. Gatski[4,e)]

[1]*Unité de Mécanique de Lille (UML), Polytech'Lille, Université de Lille, Cité Scientifique, Av. Paul Langevin, 59650 Villeneuve d'Ascq, France*

[2]*Fluid Mechanics Laboratory, Dept. of Mechanical Engineering, Federal University of Uberlândia, Campus Santa Mônica, Uberlândia, Minas Gerais, Brazil*

[3]*Mechanical Engineering Coordination, Instituto Federal do Espírito Santo, Av. Vitória, 1729, CEP 29.040-780, Vitória, ES, Brazil*

[4]*Center for Coastal Physical Oceanography, Department of Ocean, Earth and Atmospheric Sciences, Old Dominion University, Norfolk, Virginia 23529, USA*

(Received 17 January 2018; accepted 5 June 2018; published online 27 June 2018)

An analysis of the spectral turbulent kinetic energy budget in a fully developed turbulent plane channel flow is performed. Direct numerical simulation data are evaluated at friction Reynolds numbers Re_τ of 180 and 1000. The analysis is focused on the influence of the Reynolds number on the spectral cascade of energy and the corresponding energy cascade in physical space in the presence of inhomogeneity and anisotropy. The turbulent kinetic energy distribution is compared for both Reynolds numbers, and the relevant characteristics of the energy transfer process in a wall-bounded turbulent flow are described. Differences in energy cascade are noted between the Reynolds number at both low and high wavenumbers. The results of the analysis are further assessed with a comparison to an earlier study of spectral energy transfer at $Re_\tau = 180$. *Published by AIP Publishing.* https://doi.org/10.1063/1.5022653

I. INTRODUCTION

Homogeneous isotropic turbulence (HIT), exemplifying the simplest of turbulence dynamics, has been exhaustively studied for well over half a century, e.g., Comte-Bellot and Corrsin,[6] George,[11] Kolmogorov,[17] Pope,[27] Richardson,[28] Skrbek and Stalp,[31] and Tennekes and Lumley.[32] By characterizing the HIT, Richardson[28] and Kolmogorov[17] showed that, in this kind of flow, the transport of energy is accomplished only in the spectral domain, through a continuous spectrum of energy density. It was established that this continuous spectrum can be divided into three main spectral ranges: large production scales, inertial energy transfer scales, and small dissipative scales. While HIT is an important contributor to the fundamental understanding of turbulence dynamics, there are two more equally important fundamental features. These are related to the statistical behavior of the turbulence and include the anisotropy of the second- (and higher) order moments and the (spatial) inhomogeneity of the statistical field. For these purposes, here the focus will be on statistically stationary fields.

The imposition of mean flow shear onto the turbulence field alters the dynamics by introducing anisotropy into the turbulent velocity correlation field. Since the flow domain is assumed unbounded, statistical homogeneity of the turbulence is still maintained, but the resulting homogeneous sheared turbulence (HST) significantly alters the spectral cascade. A turbulent energy production mechanism is now introduced into the energy cascade. Fortunately such flows yield transport equations for the velocity second-moments that are readily amenable to analysis. Additionally, both direct numerical simulations (DNSs) and large-eddy simulations (LESs) can reproduce highly accurate time dependent simulations of such flows.

Even though the effects of anisotropy significantly increased our understanding of the flow dynamics, many engineering relevant turbulent flows involve non-slip solid boundaries such that effects of inhomogeneity are introduced. The most common flow that has been studied exhibiting such inhomogeneity is the fully developed turbulent channel flow (TCF). Solid boundaries are placed in the mean flow (streamwise) direction. Since the mean flow is fully developed and the turbulence in the streamwise direction has equilibrated, homogeneity is maintained in planes parallel to the solid boundaries and perpendicular to the direction of mean shear.

The inhomogeneity and anisotropy are responsible for the generation of an energy transfer in the physical space, where the energy sources are dependent on the distances from the wall. This combination of energy transfer mechanisms within spatial planes both parallel (inhomogeneous effects) and perpendicular (homogeneous effects) to the direction of shear suggests the need to isolate the contributions of each to the overall dynamics of the flow. In the cross-stream direction of the channel, the flow field is delimited by well-defined regions having different dynamic mechanisms that dominate in the turbulent kinetic energy balance. These regions include the viscous sub-layer, where viscosity dominates, the buffer layer, where production has its peak, the logarithmic layer,

a)joao.andrade@etudiant.univ-lille1.fr
b)ramon.martins@ufes.br
c)gilmar.mompean@polytech-lille.fr
d)laurent.thais@polytech-lille.fr
e)gatski@ccpo.odu.edu

where production is in equilibrium with dissipation, and the outer layer region, where turbulence is energized by the spatial flux of turbulent kinetic energy generated within the buffer layer.[27]

In the channel flow, the turbulent kinetic energy is produced through the interaction of the turbulent shear stress and mean shear with the maximum occurring in a buffer region at scales above the shear scale. This generated energy then cascades (forward and reverse) through a broad range of scales associated with both the viscous sub-layer and the outer bulk region of the flow. Since the energy, generated at the intermediate scales, feeds larger motions farther away from the wall,[5] a local energetic equilibrium (energy production balances the dissipation rate) can exist in a logarithmic region. This Kolmogorov hypothesis[17] on the locality of the energy transfer[9] and interacting scales[36,37] has been validated by numerical simulations whenever channel flow simulations have been performed.

This energetic transfer behavior in wall-bounded turbulent flows is an important characteristic and gives rise to a reverse energy cascade from the smaller to the larger scales, the so-called energy backscatter.[16,25]

Marati *et al.*[18] were the first to utilize simulation data of the channel flow within the structure function framework to analyze the energetic fluxes and scale energy budgets. They analyzed a DNS data set of a low Reynolds number turbulent channel flow and examined the transference of energy associated with a specific scale of motion through the spectrum of scales, and, simultaneously, how the same scale of motion exchanges energy with a properly defined spatial flux. The second order structure function was considered to develop the kinetic energy density scale-by-scale analysis.

Dunn and Morrison[10] analyzed the evolution equation for the kinetic energy density by means of the wavelet transform, which offers a relation between a spatial and a spectral description to investigate the spatial and scale-to-scale flux of turbulence kinetic energy in the turbulent channel flow at $Re_\tau = 300$.

Cimarelli *et al.*[5] studied the behavior of the energy fluxes in the spectral and physical spaces in wall-bounded turbulent flows by means of the balance equation for the second-order structure function. It has been shown by Cimarelli and De Angelis[4] that an inverse cascade energy flux mechanism acts when the turbulence is first generated in a near-to-wall region in an intermediate range of small scales. From these small scale sources, turbulent energy spreads toward larger structures in regions farthest from the wall. Then, the largest turbulent structures are converted to the smallest scales of motion and are dissipated. The authors identified two main dynamical processes as driving mechanisms for the fluxes. One, stronger, is located in the near-wall region and a second one further away from the wall. This forward and reverse cascade of the energy flux has a direct influence on the modeling of the subgrid scale stresses in large-eddy simulations. Cimarelli and De Angelis[4] proposed a mixed subgrid scale model where the backward energy transfer effects in the near–wall region are captured for very large filter lengths. Surprisingly, Gualtieri *et al.*[12] performed an LES of homogeneous sheared turbulence (HST) using an approximate deconvolution method (rather than a functional model). They found that when the energy producing scales are well resolved and the lower order statistics well captured, higher order statistics did not exhibit significant deterioration in accuracy. Nevertheless, even in this case, an enhanced knowledge of the detailed energetic spectral transfer could lead to further insights into reasons behind such surprising behavior.

In a recent important study, Mollicone *et al.*[21] have contributed a study of energy cascades in physical space using a generalised Kolmogorov equation. They extended the comprehension of the production and transfer of turbulent kinetic energy (TKE) in the combined position/scale spaces for a more complex geometry, a separation bubble generated by a bulge at a turbulent plane channel flow. The generalised Kolmogorov equation was proven to be appropriate for the understanding of the kind of complex flow.

A characterizing feature of these previous studies (Marati, Cimarelli, and Mollicone) is the utilization of the structure function partitioning originally exploited by Ref. 17 and recently formalized and generalized by Refs. 13 and 14. These structure functions are closely linked to the two-point correlation function in physical space. In the more general inhomogeneous case, an account must be taken of the separation distance between two points as well as the location in the flow field itself (in the homogeneous case, only separation distance is needed). In the study reported here, the analysis is restricted to a single-point formulation in physical space coupled with a spectral representation of the instantaneous turbulent flow field. Within this context, the turbulent flow is assumed partitioned into locally homogeneous turbulence in planes parallel to the bounding channel walls with effects of inhomogeneous mean shear dependent on distance from the channel walls. Such an approach attempts to simplify a generally complex system of energetic dynamics into a within-plane and an out-of-plane energy exchange system.

Bolotnov *et al.*[2] analyzed a direct numerical simulation of the turbulent channel flow at $Re_\tau = 178.12$ to understand the spectral turbulent kinetic energy distribution and the terms which determine the energy distribution in physical and wavenumber spaces by using DNS data from the study by Trofimova *et al.*[35]

So, in short, the description in spectral space alone is insufficient to capture the real dynamics of TCF, which differs from the HIT by the existence of two forms of energy transfer, the energy transfer in the wavenumber space and in the physical space associated with the inhomogeneity and anisotropy of the flow. Such processes are strongly scale and position dependent. In this way, a necessary task to completely describe the real dynamics, in the presence of the spatial fluxes induced by inhomogeneity, is the study of the spatial and the spectral behaviors of a turbulent plane channel flow and the impact of the Reynolds number. The simultaneous spectral/spatial analysis of the influence of the Reynolds number in the transport equation for the TKE in turbulent flow separation induced by a protuberance on one of the walls, performed by Mollicone *et al.*,[20] shows great importance, especially when

the influence of the energy flux of different scales is assessed for subgrid-scale closure models.[30]

In this context, the present paper analyzes the energy flux in the complete physical space and spectral domain, allowing the direct correlation between different wall-parallel planes, and helps to unveil new important details of the energy transfer processes. We aim to enrich this study with further analysis of the influence of the turbulent Reynolds number, helping to provide more insight into the physics of turbulent Newtonian fluid flows. The effect of the Reynolds number on the turbulent kinetic energy (TKE) transfer of Newtonian fluids at $Re_\tau = 180$ and $Re_\tau = 1000$ by means of the Fourier transform was never done before and is evaluated in detail in the present work. Various energy fluxes were analyzed for wall bounded turbulence due to both spectral and spatial energy variations.

The organization of the paper is as follows. The detailed channel flow configuration, the numerical method used, and its validation case are described in Sec. II. The spectral equations for the turbulent kinetic energy and the decomposition used can be found in Sec. III. The results are discussed in Sec. IV. Discussions and conclusion are found in Sec. V. The validation of the results by comparison with the work of Bolotnov *et al.*[2] is shown in the Appendix.

II. THE TURBULENT CHANNEL FLOW DATA

Fully developed turbulent flows of Newtonian fluids are considered. For the channel flow, the usual notations for this geometry are used; i.e., the channel streamwise direction is $x_1 = x$, the wall-normal direction is $x_2 = y$, and the spanwise direction is $x_3 = z$ with the velocity field in the respective directions $(u_1, u_2, u_3) = (u, v, w)$. The channel half-width is denoted by h, while the two other directions are considered of infinite extent.

New direct numerical simulations were conducted to provide the data used for the spectral analysis. The Navier-Stokes equations for a divergent-free velocity field were solved on a hybrid spatial scheme that includes Fourier spectral accuracy in two directions (x_1 and x_3) and sixth-order compact finite differences for first and second-order wall-normal derivatives (x_2). Time marching can be up to fourth-order accurate. Spatial averaging is taken in the two homogeneous channel directions (x_1, x_3), and a turbulent field was used as an initial condition. The full description of the employed algorithm can be found in the study by Thais *et al.*[33]

In the present paper, the direct numerical simulation of the fully developed turbulent channel flow is analyzed at $Re_\tau = 180$ and 1000, where Re_τ is the friction Reynolds number, based on the friction velocity, $u_\tau \equiv \sqrt{\tau_w/\rho}$, and the channel half-gap, h, and is defined as

$$Re_\tau = \frac{u_\tau h}{\nu}, \tag{1}$$

where ν is the kinematic viscosity, τ_w is the mean wall shear stress, and ρ is the fluid density.

The database parameters of the numerical simulations for the different Reynolds numbers are given in Table I. The presented parameters are Reynolds number, domain size, number of grid points, and mesh resolution.

TABLE I. Overview of DNS databases.

Re_τ	$L_1/h \times L_3/h$	$N_{x_1} \times N_{x_2} \times N_{x_3}$	δx_1^+	δx_{2max}^+	δx_{2w}^+	δx_3^+
180	$8\pi \times 3\pi/2$	$512 \times 129 \times 128$	8.8	7.1	0.2	6.6
1000	$6\pi \times 3\pi/2$	$1536 \times 513 \times 768$	12.3	8.4	0.5	6.1

III. MOMENTUM AND TURBULENT ENERGY EQUATIONS

A fully developed channel flow of a Newtonian fluid is analyzed. The components of the total velocity are given by $u_i = U_i + u_i$, where U_i and u_i are the mean and fluctuating velocities, respectively. The total pressure field is given by $p = P + p$, similar to the velocity decomposition, P and p are the mean and the fluctuating pressure fields, respectively. The fluctuation continuity and momentum equations are given by

$$\frac{\partial u_j}{\partial x_j} = 0, \tag{2}$$

$$\frac{\partial u_i}{\partial t} + u_j\frac{\partial u_i}{\partial x_j} + U_j\frac{\partial u_i}{\partial x_j} + u_j\frac{\partial U_i}{\partial x_j} = -\frac{\partial p}{\partial x_i} + 2\nu\frac{\partial s_{ij}}{\partial x_j}, \tag{3}$$

with $\partial p/\partial x$ being the nonzero streamwise pressure gradient driving the turbulent flow and s_{ij} being the components of the fluctuating rate-of-strain tensor.

A. Momentum equation in Fourier space

For a fully developed channel flow, a two-dimensional spatial Fourier transform pair is needed and defined here by

$$\hat{u}_i(k_1, k_2, x_2, t) = \frac{1}{(2\pi)^3}\int e^{\iota(k_1x_1+k_3x_3)}u_i(x_1, x_2, x_3, t)\mathrm{d}x_1\mathrm{d}x_3, \tag{4}$$

$$u_i(x_1, x_2, x_3, t) = \int e^{-\iota(k_1x_1+k_3x_3)}\hat{u}_i(k_1, k_2, x_2, t)\mathrm{d}k_1\mathrm{d}k_3, \tag{5}$$

where $\hat{u}_i$ are the velocity components in the Fourier domain and the wavevector components are $k_i = 2\pi/\lambda_i$, with λ_i being the wavelength components. The transformed continuity equation is

$$-\iota k_1\hat{u}_1 + \frac{\partial\hat{u}_2}{\partial x_2} - \iota k_3\hat{u}_3 = 0, \tag{6}$$

where ι is the imaginary unit. The transformed momentum equations are

$$\begin{aligned}\partial_t\hat{u}_1 + \nu\kappa^2\hat{u}_1 - \nu\frac{\partial^2\hat{u}_1}{\partial x_2^2} &= \iota k_1\hat{p} + \iota k_1\hat{u}_1U_1 - \hat{u}_2\frac{\partial U_1}{\partial x_2}\\ &\quad + \iota k_1\hat{u}_1 \star \hat{u}_1 + \iota k_3\hat{u}_3 \star \hat{u}_1\\ &\quad - \frac{\partial(\hat{u}_2 \star \hat{u}_1)}{\partial x_2},\end{aligned} \tag{7}$$

$$\begin{aligned}\partial_t\hat{u}_2 + \nu\kappa^2\hat{u}_2 - \nu\frac{\partial^2\hat{u}_2}{\partial x_2^2} &= -\frac{\partial\hat{p}}{\partial x_2} + \iota k_1\hat{u}_2U_1 + \iota k_j\hat{u}_j \star \hat{u}_2\\ &\quad + \iota k_1\hat{u}_1 \star \hat{u}_2 + \iota k_3\hat{u}_3 \star \hat{u}_2\\ &\quad - \frac{\partial(\hat{u}_2 \star \hat{u}_2)}{\partial x_2},\end{aligned} \tag{8}$$

$$\partial_t \hat{u}_3 + \nu\kappa^2\hat{u}_3 - \nu\frac{\partial^2\hat{u}_3}{\partial x_2^2} = \imath k_3\hat{p} + \imath k_1\hat{u}_3U_1 + \imath k_j\hat{u}_j \star \hat{u}_3 + \imath k_1\hat{u}_1 \star \hat{u}_3 + \imath k_3\hat{u}_3 \star \hat{u}_3 - \frac{\partial(\hat{u}_2 \star \hat{u}_3)}{\partial x_2}, \quad (9)$$

where $\kappa^2 = k_1^2 + k_3^2$. It is worth noticing that the above equations were developed for a turbulent plane channel flow. Therefore the periodicity condition required for the Fourier transform is true only in the x_1 and x_3 directions. In this way, the derivative terms in the x_2 direction remain in the physical domain.

B. Turbulent kinetic energy budget in Fourier space

The spectrum tensor components $\mathbf{\Phi}_{ij}(\mathbf{k})$ can be written as

$$\delta(\mathbf{k}-\mathbf{k}')\mathbf{\Phi}_{ij}(\mathbf{k}) = \frac{1}{2}\left[\overline{\hat{u}_i(\mathbf{k})\hat{u}_j^*(\mathbf{k}')} + \overline{\hat{u}_i^*(\mathbf{k})\hat{u}_j(\mathbf{k}')}\right] = \mathcal{R}e\left[\overline{\hat{u}_i(\mathbf{k})\hat{u}_j^*(\mathbf{k}')}\right], \quad (10)$$

with the two wavenumbers vectors $\mathbf{k} = (k_1, k_3)$ and $\mathbf{k}' = (k_1', k_3')$ and $\hat{u}_i^*(\mathbf{k}')$ is the velocity complex conjugate. The Dirac function is given by $\delta(\ )$, and $\mathcal{R}e[\ ]$ represents the real part of a complex number. The trace of $\delta(\mathbf{k}-\mathbf{k}')\mathbf{\Phi}_{ij}(\mathbf{k})$ is given by

$$\delta(\mathbf{k}-\mathbf{k}')\mathbf{\Phi}_{ii}(\mathbf{k}) = \overline{\hat{u}_i(\mathbf{k})\hat{u}_i^*(\mathbf{k}')} = \mathcal{R}e\left[\overline{\hat{u}_i(\mathbf{k})\hat{u}_i^*(\mathbf{k}')}\right]. \quad (11)$$

The turbulent kinetic energy is obtained by multiplying the momentum equations [Eqs. (7)–(9)] by its respective complex conjugate, $\hat{u}_i^*(\mathbf{k}')$, adding the result to its complex conjugate, and then averaging. Introduction of $\delta(\mathbf{k}-\mathbf{k}')\mathbf{\Phi}_{ii}(\mathbf{k})$ from Eq. (11) results in each term being infinite due to the delta-function. This can be removed integrating over $\mathbf{k}'$. The integrate sum of the momentum equations in the spectral domain can be decomposed into seven main mechanisms, yielding

$$\frac{\partial E(\kappa, x_2)}{\partial t} = \mathcal{P} - \varepsilon_{in} - \varepsilon_{out} + \mathcal{T}_{in} + \mathcal{T}_{out} + \mathcal{D}_\nu + \mathcal{D}_p, \quad (12)$$

where $\mathcal{P}$ is the turbulent production by mean shear (shear turbulent production), ε_{in} is the in-plane turbulent energy dissipation rate, ε_{out} is the inter-plane turbulent energy dissipation rate, $\mathcal{T}_{in}$ is the in-plane turbulent transport by the velocity fluctuation, $\mathcal{T}_{out}$ is the inter-plane turbulent transport, $\mathcal{D}_\nu$ is the viscous diffusion, $\mathcal{D}_p$ is the diffusion by pressure fluctuations, and the energy spectral density is given by

$$E(\kappa, x_2) = \frac{1}{2}\int_0^{2\pi} \mathbf{\Phi}_{ii}(\kappa, x_2)d\kappa_\phi = \pi\mathbf{\Phi}_{ii}(\kappa, x_2)\kappa, \quad (13)$$

with polar coordinates used in the integral evaluation (κ, κ_ϕ). It follows that in the (k_1, k_3) spectral plane each budget term in Eq. (12) can be considered as only a function of $|\mathbf{k}|$ $(= \kappa)$ with $\kappa^2 = k_1^2 + k_3^2$. The seven terms on the right-hand side of Eq. (12) are functions only of $|\mathbf{k}|$ and x_2.

The nomenclature involved here is based on the work of Bolotnov *et al.*,[2] where the terms with derivatives in the wall-normal direction $(\partial/\partial x_2)$ are named inter-plane terms and are represented by the subscript "out" that means "out-of-plane." The terms with derivatives in the homogeneous $x_1 - x_3$ plane $(\partial/\partial x_1$ and $\partial/\partial x_3)$ are named in-plane terms and are represented by the subscript "in."

The turbulent production is given by

$$\mathcal{P}(\mathbf{k}, x_2) = -\frac{1}{2}\frac{\partial U_1}{\partial x_2}\left[\overline{\hat{u}_1^*(\mathbf{k})\hat{u}_2(\mathbf{k})} + \overline{\hat{u}_1(\mathbf{k})\hat{u}_2^*(\mathbf{k})}\right]. \quad (14)$$

The in-plane turbulent energy dissipation rate is

$$\varepsilon_{in}(\mathbf{k}, x_2) = 2\nu\kappa^2 E(\kappa, x_2). \quad (15)$$

The inter-plane turbulent energy dissipation rate is given by

$$\varepsilon_{out}(\mathbf{k}, x_2) = \nu\left[\overline{\frac{\partial\hat{u}_i^*(\mathbf{k})}{\partial x_2}\frac{\partial\hat{u}_i(\mathbf{k})}{\partial x_2}}\right]. \quad (16)$$

The in-plane turbulent transfer is

$$\mathcal{T}_{in}(\mathbf{k}, x_2) = \frac{\imath k_1}{2}\left\{\overline{\hat{u}_m^*(\mathbf{k})[\hat{u}_1 \star \hat{u}_m]|_\mathbf{k}} - \overline{\hat{u}_m(\mathbf{k})\left[\hat{u}_1^* \star \hat{u}_m^*\right]|_\mathbf{k}}\right\} + \frac{\imath k_3}{2}\left\{\overline{\hat{u}_m^*(\mathbf{k})[\hat{u}_3 \star \hat{u}_m]|_\mathbf{k}} - \overline{\hat{u}_m(\mathbf{k})\left[\hat{u}_3^* \star \hat{u}_m^*\right]|_\mathbf{k}}\right\}. \quad (17)$$

The inter-plane turbulent transfer is

$$\mathcal{T}_{out}(\mathbf{k}, x_2) = -\frac{1}{2}\left\{\overline{\hat{u}_m^*(\mathbf{k})\frac{\partial}{\partial x_2}[\hat{u}_2 \star \hat{u}_m]|_\mathbf{k}} + \overline{\hat{u}_m(\mathbf{k})\frac{\partial}{\partial x_2}\left[\hat{u}_2^* \star \hat{u}_m^*\right]|_\mathbf{k}}\right\}. \quad (18)$$

The viscous diffusion term is given by

$$\mathcal{D}_\nu(\mathbf{k}, x_2) = \nu\frac{\partial^2 E(\kappa, x_2)}{\partial x_2^2}. \quad (19)$$

The pressure diffusion is

$$\mathcal{D}_p(\mathbf{k}, x_2) = -\frac{1}{2}\frac{\partial}{\partial x_2}\left[\overline{\hat{u}_2^*\hat{p}} + \overline{\hat{u}_2\hat{p}^*}\right]. \quad (20)$$

In this two-dimensional shear flow, there is a planar homogeneity introduced in both the streamwise and spanwise directions. For the spectral function, $\mathbf{\Phi}_{ii}(\mathbf{k}, x_2)$, the integration over the circumference in spectral space is given by

$$K(x_2) = \frac{1}{2}\int_{|\mathbf{k}|=\kappa} \mathbf{\Phi}_{ii}(\mathbf{k}, x_2)d\mathbf{k} = \int_\kappa E(\kappa, x_2)d\kappa. \quad (21)$$

In part of the Bolotnov *et al.*[2] analysis, the spectrum was partitioned into wavenumber bands that were organized into m(=24) bins. In the current study, $m = 28$ and Eq. (22) can be written as

$$K_m(x_2) = \pi\int_{\kappa_{m-1}}^{\kappa_m} \mathbf{\Phi}_{ii}(\kappa, x_2)\kappa d\kappa \simeq \pi\mathbf{\Phi}_{ii}(\overline{\kappa}_m, x_2)\overline{\kappa}_m\Delta\kappa_m, \quad (22)$$

where $\bar{\kappa}_m = 0.5(\kappa_{m-1} + \kappa_m)$ is an average wavenumber contained within bin-m, $\Delta\kappa_m = \kappa_m - \kappa_{m-1}$ is the spectral width of bin-m, and K_m is the turbulent kinetic energy contribution from the spectral band associated with bin-m.

By integrating Eq. (12) over κ, the transport equation for the TKE in physical space is obtained

$$\frac{DK(x_2)}{Dt} = -\overline{u_iu_j}\frac{\partial U_i}{\partial x_j} - \nu\overline{\frac{\partial u_i}{\partial x_j}\frac{\partial u_i}{\partial x_j}} - \frac{1}{\rho}\frac{\partial\overline{u_ip}}{\partial x_i} - \frac{1}{2}\frac{\partial\overline{u_ju_ju_i}}{\partial x_i} + \nu\frac{\partial^2 K}{\partial x_j^2}, \quad (23)$$

where the five terms on the right-hand side, depending only on x_2, are the usual terms representing, respectively, production by mean shear, total energy dissipation rate, pressure diffusion, total turbulent transport, and viscous diffusion.

The spectral results presented in the current paper were normalized with two different procedures, which are termed global and local normalization.[2] The global normalization is a common normalization of all terms on the right-hand side of Eq. (12) and is based on the fluid viscosity and friction velocity of the flow

$$\theta^+(\kappa, x_2) = \left(\frac{\nu}{u_\tau^4}\right)\theta(\kappa, x_2), \tag{24}$$

where θ is a generic variable and can assume any of the source term functions. The globally normalized source terms are marked with superscript "+." The non-dimensional turbulent kinetic energy density is defined as

$$E^+ = E/(u_\tau \nu). \tag{25}$$

The local normalization expresses the spectral shape of the source based on its magnitude. In this normalization, the variable is integrated over the whole wavenumber range at each x_2 location and is given by

$$\hat{\theta} \equiv \frac{\theta^+}{\theta^*}, \tag{26}$$

where

$$\theta^*(x_2) = \int_{\kappa^+} |\theta^+(\kappa^+, x_2)| d\kappa^+, \tag{27}$$

where $\kappa^+ = (\nu/u_\tau)\kappa$ is the dimensionless wavenumber scaled by wall coordinates. The dimensionless distance from the wall in wall units (y^+) is given by

$$y^+ = \frac{x_2 u_\tau}{\nu}. \tag{28}$$

Similar to Eq. (22), the source terms can be integrated over wavenumber bands (bins) and are given by

$$\theta_m^+ = \int_{\kappa_{m-1}^+}^{\kappa_m^+} \theta^+(\kappa^+) d\kappa^+, \tag{29}$$

where θ is a generic variable and can assume any source term.

IV. RESULTS

In this paper, we have explored DNS of a fully developed turbulent channel flow of the Newtonian fluid at two different Reynolds numbers Re_τ = 180 and 1000. To compute the various source terms of the energy transfer process [Eq. (12)], several instantaneous three-dimensional velocity flow fields are required. The terms of Eq. (12) were computed by using DNS data in the form of snapshots. A total of 105 snapshots during 1050 s of simulation were used for $Re_\tau = 180$, and 460 snapshots during 92 s were used for Re_τ = 1000. In wall units, the sampling time is given by $Tu_\tau/h = 67.5$ and 4.7 at Re_τ = 180 and 1000, respectively. These values represent, respectively, $\approx 50 L_x/U_b$ and $\approx 6 L_x/U_b$. In the present work, we have focused on the spatial/spectral analysis at a selection of homogeneous planes. According to Marati *et al.*,[18] temporally uncorrelated configurations are needed to obtain reliable statistics. According to Oliver *et al.*,[23] to reduce the correlation, the samples used to compute statistics are sometimes taken "far" apart in time and then treated as independent, it can lead to underestimated uncertainty if the snapshots are not sufficiently separated. Hence, it is necessary that the time snapshots be sufficiently separated and independent, at a fixed spatial point, this requires that the time separation be such that the two-point time correlation of the random variables be small. Since the low Reynolds number cases are dominated by large structures which have long time constants, it is reasonable that the 180 case has a snapshot separation time much larger than the 1000 case.

First, in Fig. 1, we present the Kolmogorov time and length scales depending on the distance from the wall at $Re_\tau = 180$ and 1000, both are in wall units. Good match is found between our results and those of Marati *et al.*[18] at Re_τ = 180. In Figs. 1(c) and 1(d), we present comparisons between the Kolmogorov length scale and the grid resolution in the x_2-direction applied in the present work. It is apparent that the orders of the smallest length and time scales are respected in the present simulation and the parameters are sufficient to achieve a well-resolved DNS. Since it is required that the smallest resolved length scale is of $O(\eta)$.[19]

Comparison of the total turbulent kinetic energy [Eq. (21)] and the ratio of production to dissipation between the present paper and results of Moser *et al.*,[22] Del Álamo *et al.*,[8] and Thais *et al.*[34] are shown in Fig. 2, where statistical quantities were calculated directly from the spatially averaged quantities with no reconstruction from the spectral domain.

From Fig. 2(a), at Re_τ = 180, the present result is in good agreement with that of Del Álamo *et al.*[8] At Re_τ = 1000, the maximum occurs at the same y^+ location as Re_τ = 180, at a slightly higher value. Figure 2(b) shows the same behavior for all the Reynolds numbers up to $y^+ \approx 80$. The lines reach a peak at $y^+ \approx 12$ and then decline followed by a bottoming until the center of the channel. An expected behavior for the high-Reynolds number channel flows is that the production and dissipation of turbulent kinetic energy will be approximately balanced in the log region. From the present results, the ratio of production to dissipation is about one over the range $50 < y^+ < 350$. In particular, at Re_τ = 1000, the ratio is closer to one than at Re_τ = 180. At Re_τ = 180, since it is a low Reynolds number, the log layer region is narrow and the region where production balancing dissipation holds is restricted.

The TKE balance across the channel half-width is shown in Fig. 3 at Re_τ = 180 and 1000. Its calculation was computed from the summing over all κ^+ of each spectral term of Eq. (12), that is,

$$\theta_t^+(y^+) = \int_{\kappa^+} \theta^+(\kappa^+, y^+) d\kappa^+, \tag{30}$$

where each term of Eq. (12) is integrated across the entire wavenumber spectrum and becomes function only of y^+ [Eq. (23)]. The dynamic balance depending on the distance from the wall is well-known and presented here for validation. For both Reynolds numbers, Re_τ = 180 and 1000, there is a peak of turbulent production located at $y^+ \approx 12$ and the balance between viscous diffusion and turbulent energy dissipation rate is evident. The pressure transport plays a relatively minor role. Both components of the energy dissipation

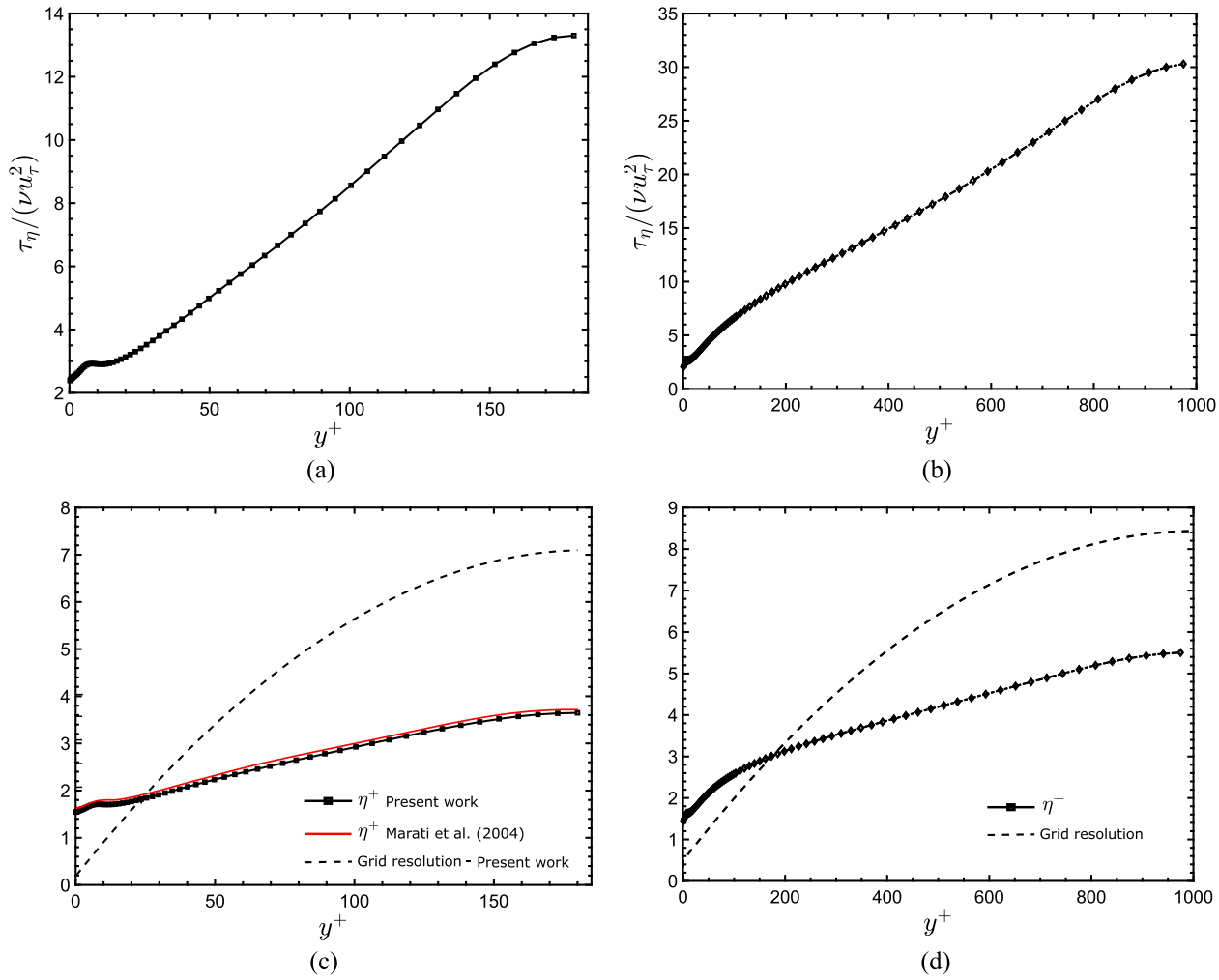

FIG. 1. The Kolmogorov scale vs. distance from the wall y^+ at $Re_\tau = 180$ and $Re_\tau = 1000$. [(a) and (b)] The Kolmogorov time scale normalized by the inner time scale (ν/u_τ^2) at $Re_\tau = 180$ and 1000, respectively; [(c) and (d)] the length scale in the wall unit and grid resolution in the x_2-direction at $Re_\tau = 180$ and 1000, respectively. Comparisons are established with Ref. 18 at $Re_\tau = 180$.

rate are negative, as expected. The rate of inter-plane dissipation makes a significant contribution to the overall balance across the whole wall-distance y^+ with a maximum value at the wall. On the other-hand, the in-plane dissipation component reaches a peak at $y^+ \approx 15$ and tends to zero elsewhere. For the turbulent transport, for $y^+ < 9.9$ there is a competition

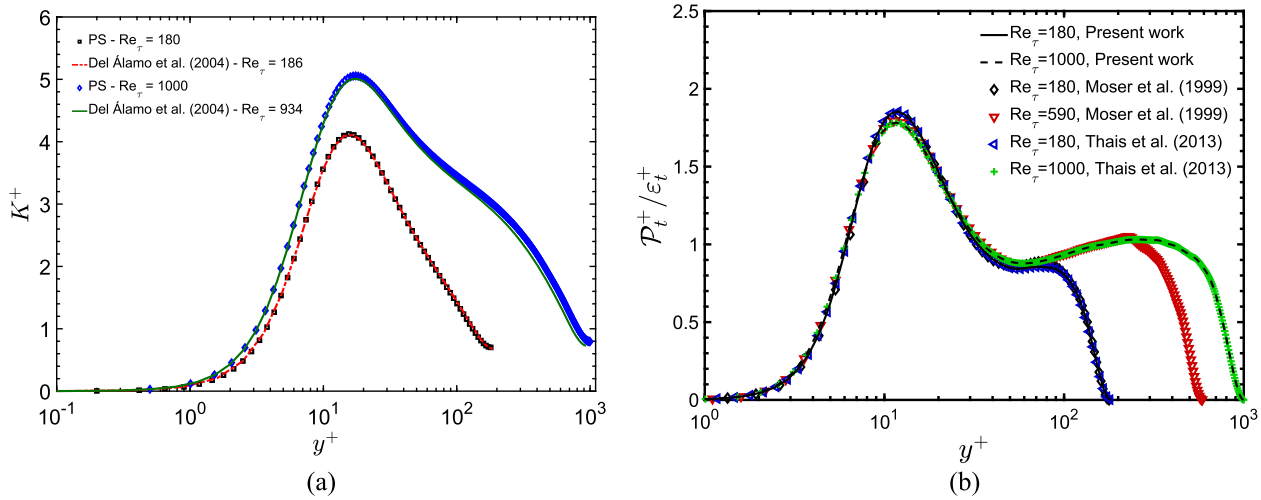

FIG. 2. Comparisons with results of Moser *et al.*,[22] Del Álamo *et al.*,[8] and Thais *et al.*[34] (a) Total turbulent kinetic energy dependence on the normalized distance from the wall and (b) ratio of production to dissipation of turbulent kinetic energy.

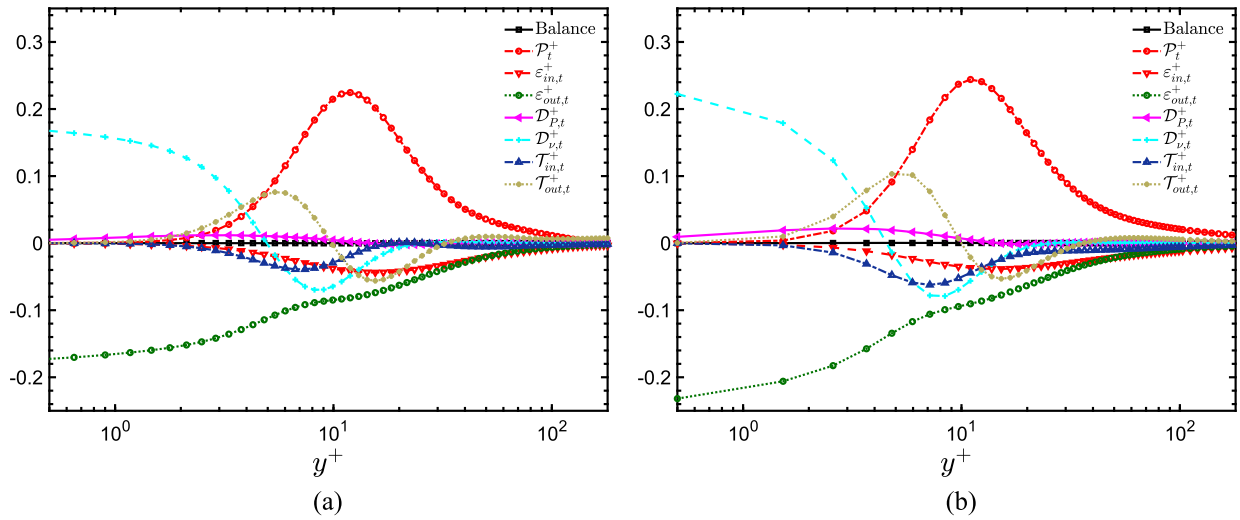

FIG. 3. Turbulent kinetic energy budget [Eq. (23)] at $Re_\tau = 180$ and 1000, respectively.

between both terms, for which the in-plane turbulent transport is negative and the inter-plane turbulent transport is positive, whereas for $y^+ > 9.9$, both terms are negative and become a sink of energy. The residual is referenced in the figure as "Balance."

In order to understand the role of each term in terms of spatial influence, the channel half-width is divided into four distinct regions (e.g., Ref. 27): I—viscous sub-layer ($y^+ < 5$), II—buffer layer ($5 < y^+ < 30$), III—log-law region ($y^+ > 30$, $y/h < 0.3$), and IV—outer layer ($y^+ > 50$).

Seeking to look into the differences between the in- and inter-plane energy dissipation rate, Fig. 4 shows both terms as well as its sum, compared to the results of Moser *et al.*[22] and Thais *et al.*[34] Although there is a difference between $Re_\tau = 180$ and 1000, both results present a similar behavior. The total energy dissipation rate is in good agreement with the reference results. At $Re_\tau = 1000$, one can notice that the ratio of inter-plane to in-plane dissipation is higher than at $Re_\tau = 180$. Discrepancies between the total dissipation of the present work and the one obtained by Thais *et al.*[34] at $Re_\tau = 1000$ are noticed. This difference can be a consequence of the calculation procedure established to compute these statistics, for which the data are first decomposed to a partially Fourier domain (wall parallel directions) and, then, we reconstruct from the spectral domain the averaged quantities through an integration process over the wavenumber [Eq. (30)]. Since the κ^+ range is (numerically) limited, the integration process does not reach the complete wavenumber bandwidth necessary to restore the terms again to the physical domain and information is lost in this procedure. These deviations come from the post-processing procedure and do not compromise the analysis of the results.

As noticed in Fig. 4, the inter-plane dissipation rate is dominant and dictates the total dissipation close to the wall (region I). This behavior comes from the fact that the velocity gradient is maximum at this location, while the in-plane

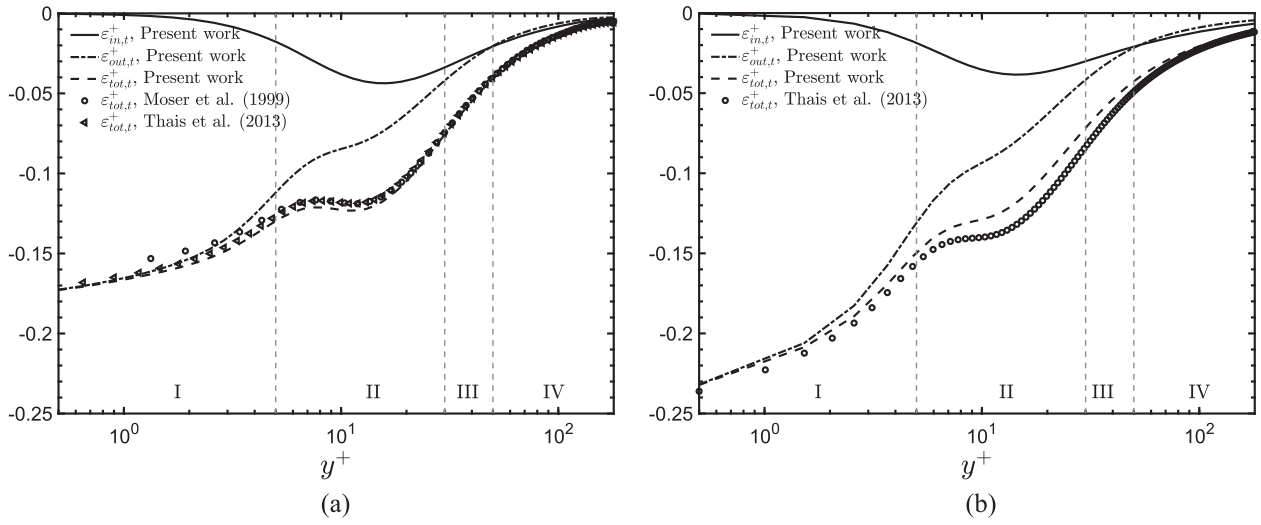

FIG. 4. In-plane, $\varepsilon_{in,t}^+$, and inter-plane, $\varepsilon_{out,t}^+$, dissipation contributions to the total dissipation, $\varepsilon_{tot,t}^+$, at $Re_\tau = 180$ and 1000, respectively. Comparisons with results of Moser *et al.*[22] and Thais *et al.*[34]

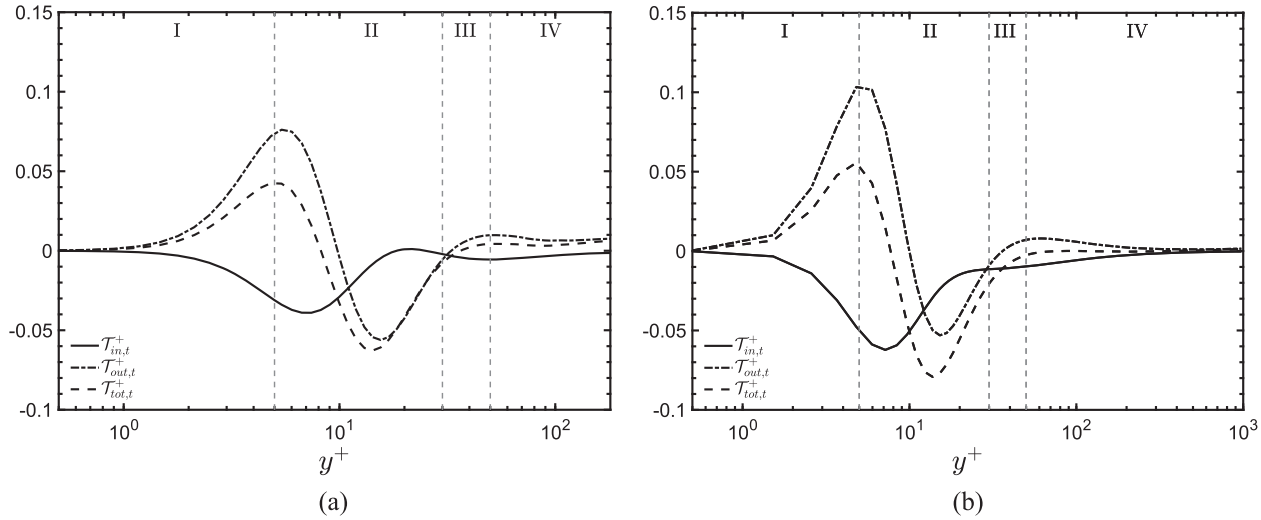

FIG. 5. In-plane, $\mathcal{T}^+_{in,t}$, and inter-plane, $\mathcal{T}^+_{out,t}$, non-linear transfer contributions to the total non-linear transfer, $\mathcal{T}^+_{tot,t}$, at $Re_\tau = 180$ and 1000, respectively.

dissipation is negligible due to the behavior of K^+ (cf. Fig. 2). The in-plane dissipation has a peak at $y^+ \approx 12$ (region II), where TKE and production are maximum (cf. Figs. 2 and 3). At the outer-layer, region IV, $\varepsilon^+_{in,t}$ becomes dominant and this behavior is maintained up to the mid-channel region. The inter-plane dissipation is higher at $Re_\tau = 1000$, while the in-plane dissipation presents similar values at both Reynolds numbers.

It is also relevant to understand the differences between the in- and inter-plane turbulent transfer rate, whose behavior and sum are presented in Fig. 5. Two peaks of total transfer are noticed in the plot. The first one, positive, is located at $y^+ \approx 5$, and the second, negative, is located at $y^+ \approx 12$. They are both dominated by the inter-plane transfer term. In region I, in-plane transfer acts as a sink of energy and the inter-plane term acts as a source, but this behavior is inverted in region II. At $Re_\tau = 1000$, due to its broad log-law layer, the in- and inter-plane terms tend to zero in the center of the channel. While at $Re_\tau = 180$, as a consequence of the narrow log-law layer, the inter-plane transfer contributes to a non-zero turbulent transfer close to the channel centerline, this behavior was also noticed by Bolotnov *et al.*[2] In region IV, the in- and inter-plane transfer will be approximately balanced. It is important to point out that the simulations were run with appropriate mesh resolution, time step, and averaging time. However, when it comes to the post-processing, a reduced number of grid points are considered in the wall normal direction since the number of discretized points in the simulation grid would be unnecessary to the developed analysis.

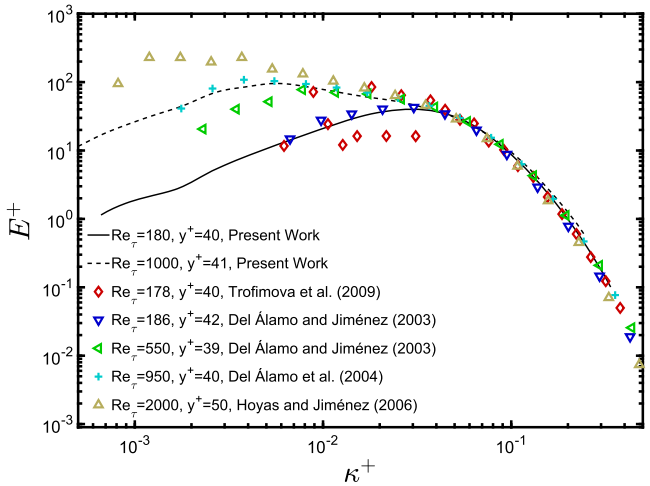

FIG. 6. Energy spectrum density at $y+ \approx 40$: present results compared to DNS data from Del Álamo and Jiménez,[7] Del Álamo *et al.*,[8] Hoyas and Jiménez,[15] and Trofimova *et al.*[35]

It is interesting to compare the energy spectrum density at a fixed position from the wall ($y^+ \approx 40$) at several Reynolds numbers (Fig. 6). Note that the spectral densities are normalized here using wall units. As shown in Fig. 6, the results at higher wavenumbers ($\kappa^+ \geq 3 \times 10^{-2}$) coincide. However, at lower κ^+, each result presents a different behavior depending on the Reynolds number.

According to Marati *et al.*,[18] since the inhomogeneity present in near-wall turbulence creates energy fluxes in the spatial domain that correspond to the spatial redistribution of turbulent kinetic energy, it is worth analyzing the spatial variation of turbulent kinetic energy spectrum density at various y^+ locations (Fig. 7). The spectra are given for 8 wall-normal positions extending from the wall to the channel center. A first observation that can be established is the fact that the spectral band for $Re_\tau = 1000$ ($5 \times 10^{-4} \geq \kappa\eta \geq 1$) is wider than that of $Re_\tau = 180$ ($1 \times 10^{-3} \geq \kappa\eta \geq 1$), where η is the Kolmogorov length scale.[26] At a higher Reynolds number, at the mid-channel region, the energy spectrum density matches the $-5/3$ slope of the inertial subrange in the region $2 \times 10^{-2} \geq \kappa\eta \geq 2 \times 10^{-1}$, which can be taken as an indication of an approach to local isotropy. On the other hand, closer to the wall, the spectrum shape is more distributed along $\kappa\eta$ and is less intense indicating the constriction of larger scales in this region.

Figure 8 shows the in-plane and inter-plane dissipation rate contributions to the total dissipation in the middle of the channel depending on the wavenumber. In an isotropic and

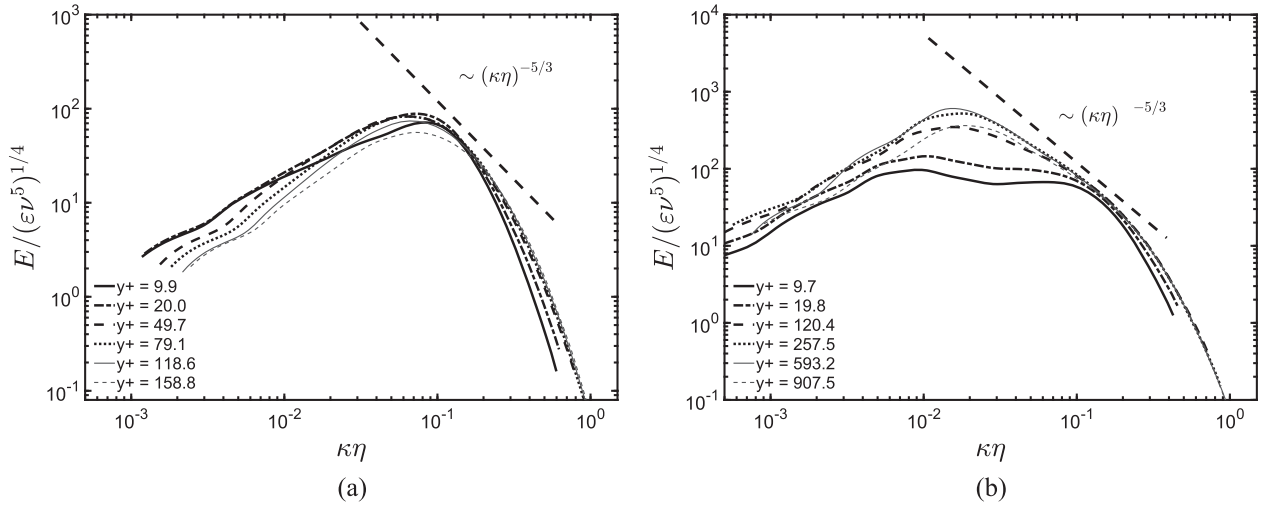

FIG. 7. Non-dimensional energy spectrum density $E/(\varepsilon\nu^5)^{1/4}$ at various y^+ locations at $Re_\tau = 180$ and 1000, respectively.

homogeneous turbulent flow,[32] the total energy dissipation rate spectrum density should match the 1/3 slope in the inertial subrange, that is, close to the mid-channel region. This behavior is more evident at $Re_\tau = 1000$. It can also be noticed that each term (in-plane and inter-plane) dominates the total dissipation rate at a different range. The inter-plane is more influential at small $\kappa\eta$, i.e., $\kappa\eta \leq 0.045$ at $Re_\tau = 180$ and $\kappa\eta \leq 0.02$ at $Re_\tau = 1000$, while the in-plane dissipation dominates at higher wavenumbers. The geometric symmetry at the channel centerline would preclude any cross-plane transfer at the centerline itself. As the centerline is approached only smaller scale in-plane motions can contribute to the energetic dynamics.

A. Spectral density of source terms to the TKE

In Figs. 9–18, a comparison between $Re_\tau = 180$ and 1000 of the spectral density of the various source terms on the right-hand side (RHS) of Eq. (12) as a function of $\kappa\eta$ is shown. The terms are normalized according to Eq. (24).

The turbulence production spectral density [Eq. (14)] is shown in Fig. 9. The significant influence of the increased Reynolds number is evident. At $Re_\tau = 1000$, the range of affected spectral scales increases with distance from the wall relative to the $Re_\tau = 180$ flow. Nevertheless, in both cases there is a shift in the location of the peak of energy production toward larger scales ($\kappa\eta$ decreases) of motion with increasing distance from the wall. This behavior comes from the fact that close to the wall, the largest scales are spatially restricted. This fact results in the observed shift in the production spectrum. Associated with this shift is a significant increase in the peak energy production level at the lower wavenumber range especially as the channel centerline is approached. At the higher wavenumbers in close proximity to the wall, the energy production at both low and high Reynolds numbers is similar. This suggests a relatively small change with the Reynolds number in energy being supplied to the small scale motions near the wall.

The in-plane dissipation rate spectral density [Eq. (15)] is presented in Fig. 10. Similar to the spectral contribution

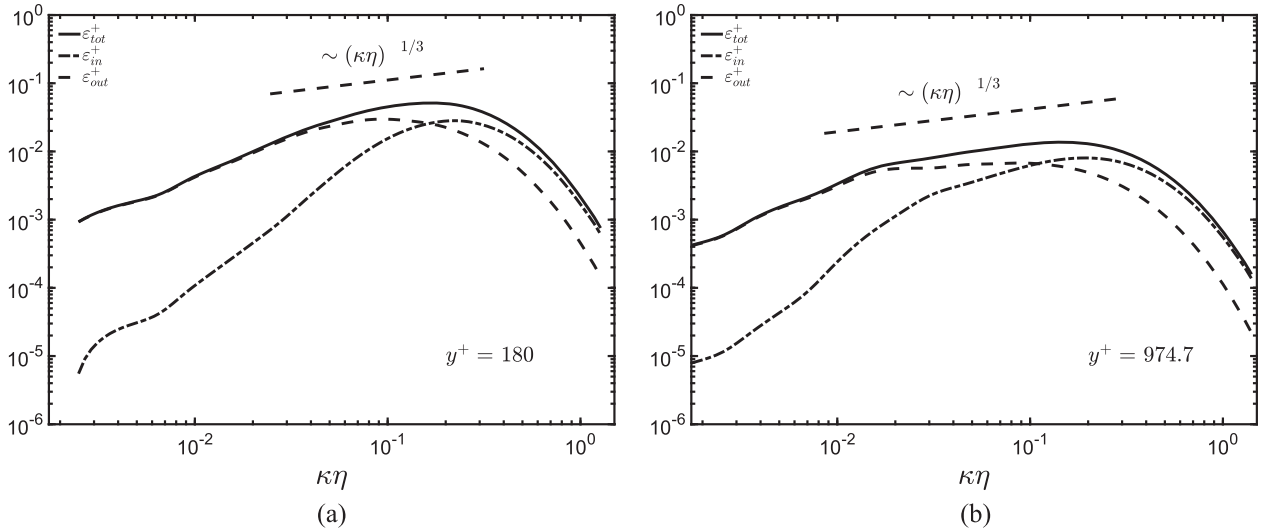

FIG. 8. Turbulent dissipation spectra in the middle of the channel at $Re_\tau = 180$ and 1000, respectively.

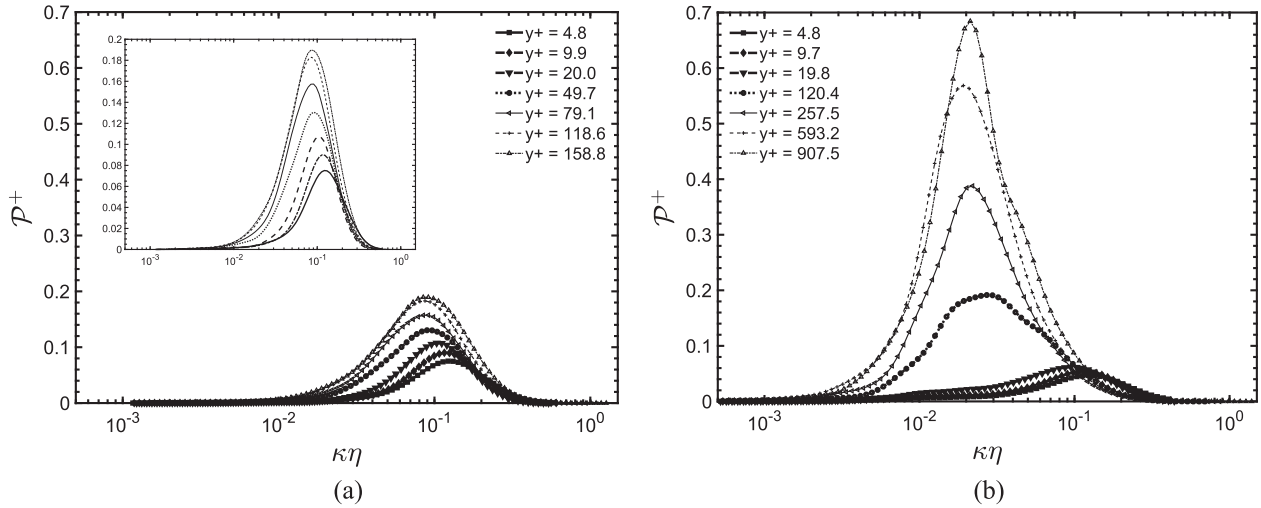

FIG. 9. Turbulent production spectral density, $\mathcal{P}^+$, at various y^+ locations at $Re_\tau = 180$ and 1000, respectively.

from production, there is a broadening of the affected spectral range with increasing distance from the wall. However, unlike the spectral contribution from production, there is a relatively minor shift in the $\kappa\eta$ location of peak intensity values across the channel. From Fig. 9, there was a monotonic increase in peak intensity with wall distance across most of the channel half-width. This behavior is not replicated with the in-plane dissipation rate spectral density. For $Re_\tau = 180$, the peak intensity levels decrease overall through the sublayer and the buffer layer regions. As y^+ increases, the peak intensity values increase with a shift to higher wavenumbers. This trend is similar for the $Re_\tau = 1000$ case, although this shift in peak intensity location is less evident. In this outer layer region, the peak intensity levels and spectral locations are the same at both Re_τ. In the inner layer region, the peak intensity levels of the in-plane dissipation rate are lower for $Re_\tau = 1000$. This indicates that in this inner layer other contributors to the spectral energy budget significantly impact the energy cascade process. It is interesting to note that, at $Re = 1000$, we have very good separation between the dissipation and production peaks, promoting a well-defined inertial region.

The inter-plane dissipation rate spectral density [Eq. (16)] is shown in Fig. 11. There is a decrease in peak intensity values for both Reynolds numbers through the wall region through $y^+ \leq 50$. In the $Re_\tau = 1000$ case, two local peak intensities in the inter-plane dissipation are observed. The results in Fig. 10 suggest no affect on the in-plane dissipation contribution, whereas, for $Re_\tau = 1000$ they show that the wall-normal spatial variations inherent in the inter-plane dissipation are influenced. In the region farther away from the wall, the intensity levels increase with a slight shift to higher wavenumbers. Most notably, there is large spectral broadening at all y^+ locations for $Re_\tau = 1000$ which is skewed toward the lower wavenumbers. Since these lower wavenumbers are associated with the larger scale motions in the flow, the inter-plane dissipation rate has a broader influence on both the physical and spectral scales across the flow compared to the in-plane contribution.

Since a second peak of the inter-plane dissipation rate is found in the close-to-wall region at $Re_\tau = 1000$, it is convenient

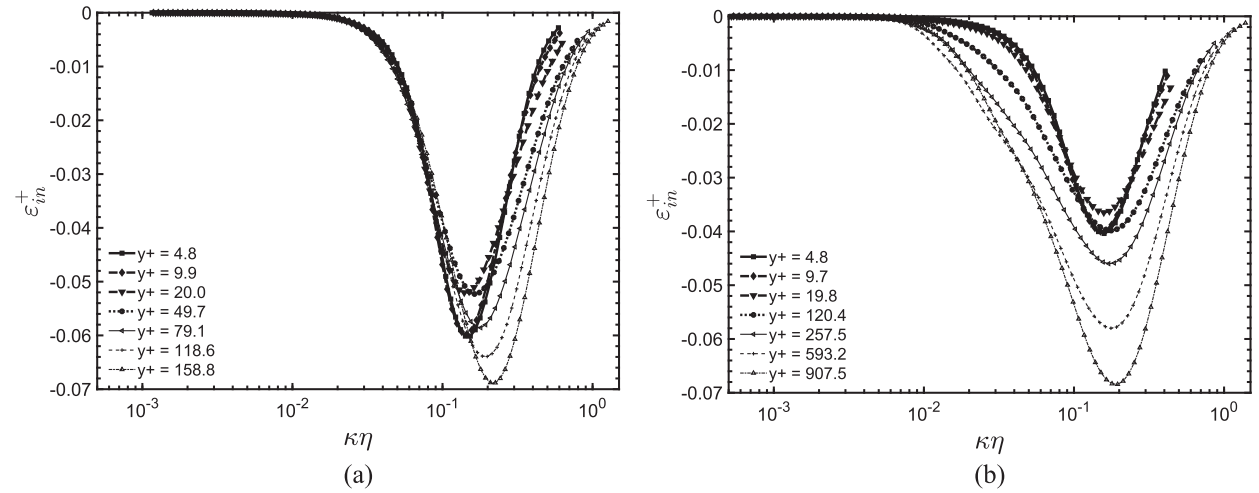

FIG. 10. In-plane dissipation spectral density, ε_{in}^+, at various y^+ locations at $Re_\tau = 180$ and 1000, respectively.

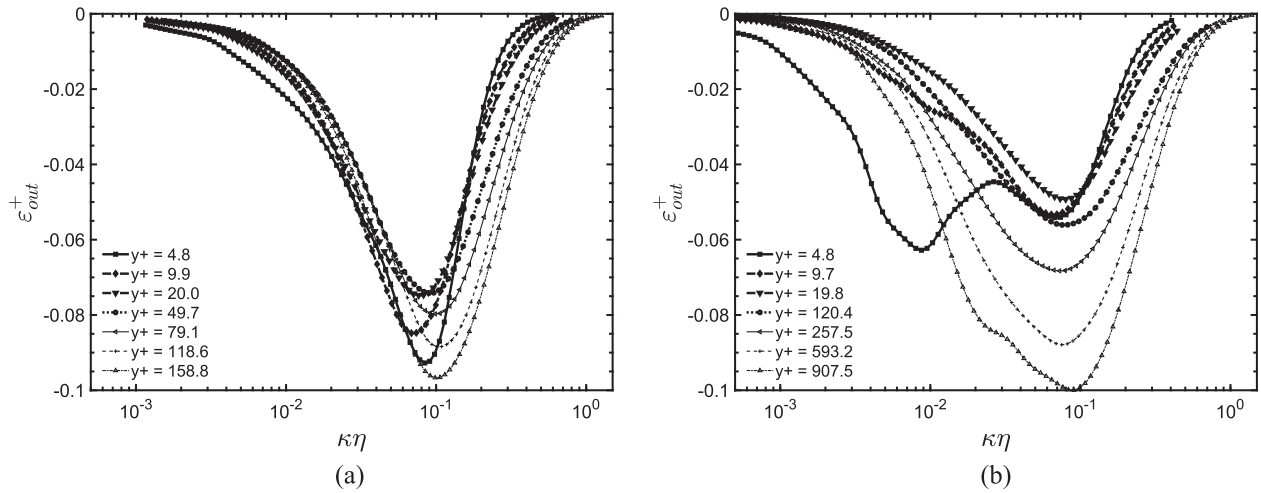

FIG. 11. Inter-plane dissipation spectral density, ε^+_{in}, at various y^+ locations.

to analyze more specifically its behavior within the viscous sub-layer and in the initial region of the buffer layer. For this purpose, Fig. 12 presents ε^+_{out} at various y^+ locations restricted to regions I and II. Two peaks are noticed in the vicinity of the wall only at $Re_\tau = 1000$, indicating that this phenomenon does not occur at low Reynolds numbers. In close proximity of the wall, both ejections and sweeps of fluid occur. This action results in the production of energy at finer scales of motion. At $Re_\tau = 180$, only one peak intensity is observed at $y^+ = 4.8$ due to the stronger influence of viscous effects at this low Reynolds number (cf. Fig. 17). For both Reynolds numbers, at low wavenumbers ($\kappa\eta < 4 \times 10^{-2}$), ε^+_{in} intensity increases for y^+ values through $y^+ \leq 2.5$ and then decreases in value with increasing distance from the wall. It seems likely that at this close wall proximity location any change in spectral behavior would be affected by the diminished effect of viscosity with the distance from the wall. An increase in the energetics at a higher Reynolds number is consistent with this thinking. The appearance of a double peak may simply be an intermediate effect at this one Re (=1000) so that at higher Re only one peak would be present and that would be at the higher $\kappa\eta$.

It is also interesting to discuss the ratio of production spectral density to total dissipation spectral density depending on both y^+ and $\kappa\eta$. It is known that the ratio $\mathcal{P}^+_t/\varepsilon^+_{tot,t}$ is close to 1 in the log-layer and is approximately 1.8 in the area where the peak of production occurs (Fig. 2). The objective here is to understand which spectral modes dominate in each region. The ratio $\mathcal{P}^+/\varepsilon^+$ is presented in Fig. 13. In the viscous sub-layer, the behavior is the same comparing the two Reynolds numbers, and monotonic increases in the log and buffer layer are found. As y^+ increases, the intensity peak shifts toward smaller wavenumber. It can be noticed that the dissipation is more important than production at higher wavenumber and it inverts as $\kappa\eta$ decreases.

Figure 14 shows the scaled in-plane non-linear transfer spectral density [Eq. (17)]. For $Re_\tau = 180$, the transfer is negative at lower wavenumber values and positive at higher

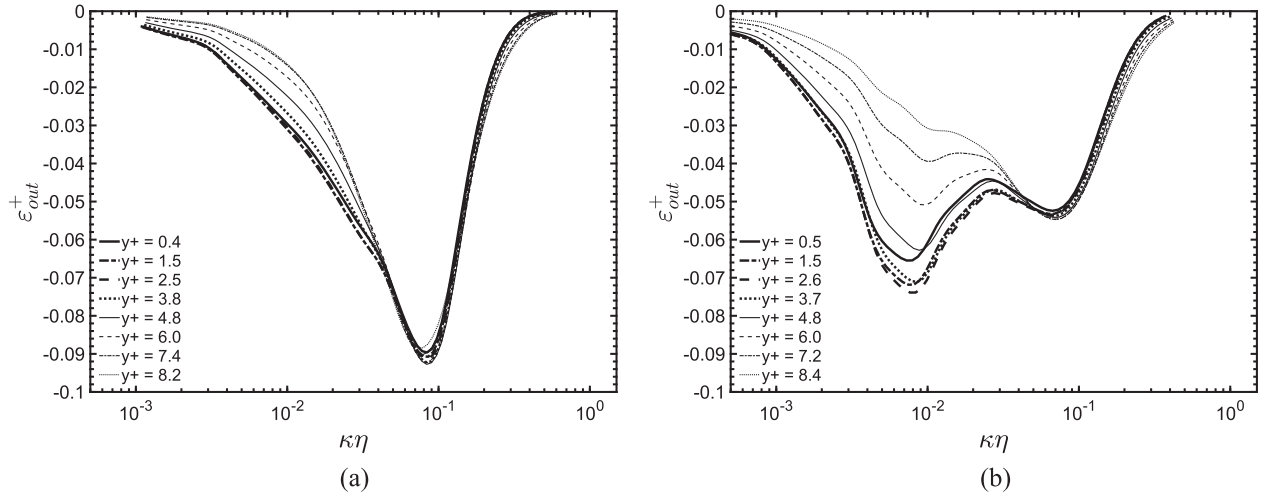

FIG. 12. Inter-plane dissipation spectral density, ε^+_{out}, at various y^+ locations in the viscous sub-layer and in the initial region of the buffer layer at $Re_\tau = 180$ and 1000, respectively.

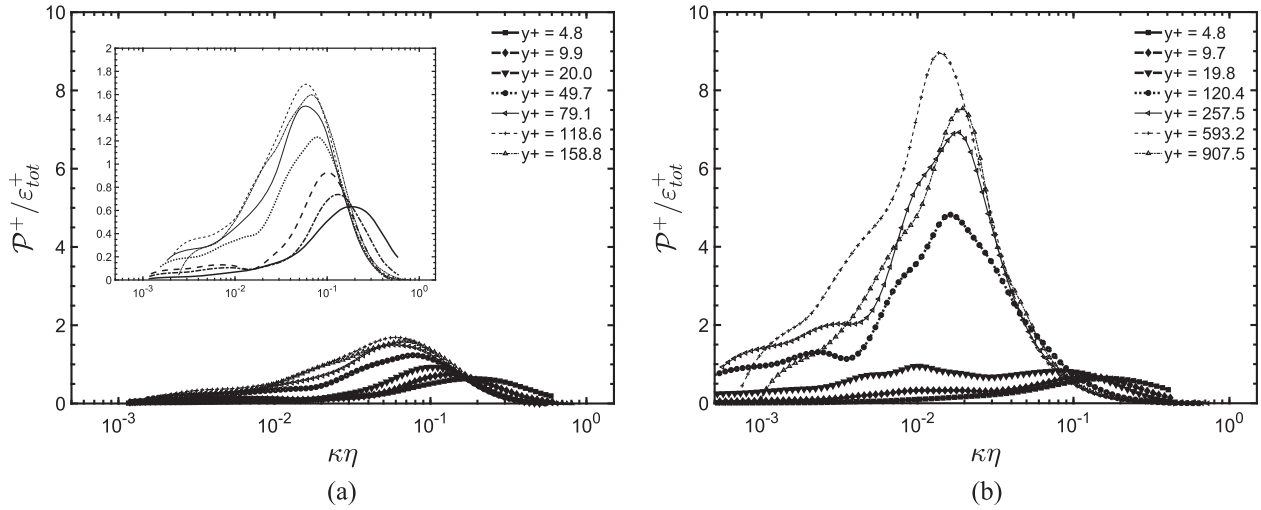

FIG. 13. Ratio of production to total dissipation spectral density at various y^+ locations at $Re_\tau = 180$ and 1000, respectively.

wavenumbers. This affirms the usual transfer of energy from larger to smaller scales in the flow. There is a shift in the $\kappa\eta$ location of both the maximum and minimum in-plane values with distance from the wall. The shift tends to larger scales for wall distances through the buffer layer and to smaller scales for the remainder of the channel half-width. For $\kappa\eta\mathcal{T}^+_{in} < 0$, peak intensity decreases for y^+ values through the buffer layer and then increase in value with increasing distance from the wall. For $\kappa\eta\mathcal{T}^+_{in} > 0$, peak intensity increases for y^+ values through the buffer layer and then decrease in value with increasing distance from the wall. This behavior is in accordance with the characteristic of this term to transfer energy from the inertial subrange (generated by the production term) into the high wavenumber range (dissipation region).

In contrast to the $Re_\tau = 180$ case, the relevant spectral range covered by the scaled in-plane non-linear transfer spectral density increases for $Re_\tau = 1000$. Additionally, in the region where the energy is transferred from the larger scales ($\kappa\eta\mathcal{T}^+_{in} < 0$) the magnitude of the non-linear spectral density is smaller than its $Re_\tau = 180$ counterpart. For the higher wavenumber contributions ($\kappa\eta\mathcal{T}^+_{in} > 0$), the relative magnitudes of non-linear spectral density between Reynolds numbers are similar. This spectral broadening is consistent with the fact that, as the Reynolds number increases in the wall-bounded flow, a wider range of spatial scales (structures) is observed. While the $\kappa\eta$ locations of the maximum and minimum non-linear spectral density distributions are generally consistent with the $Re_\tau = 180$ locations, a shift to lower wavenumbers is observed for the spectral density distributions near the channel centerline. This implies the presence of larger scale motions in the bulk flow relative to the lower Re_τ case.

As with the spectral dissipation rate, there is an additional contribution to the non-linear transfer spectral density that accounts for the inter-(spatial) plane non-linear transfer spectral density. When combined with the in-plane results, the total effect of this non-linear transfer term on the flow

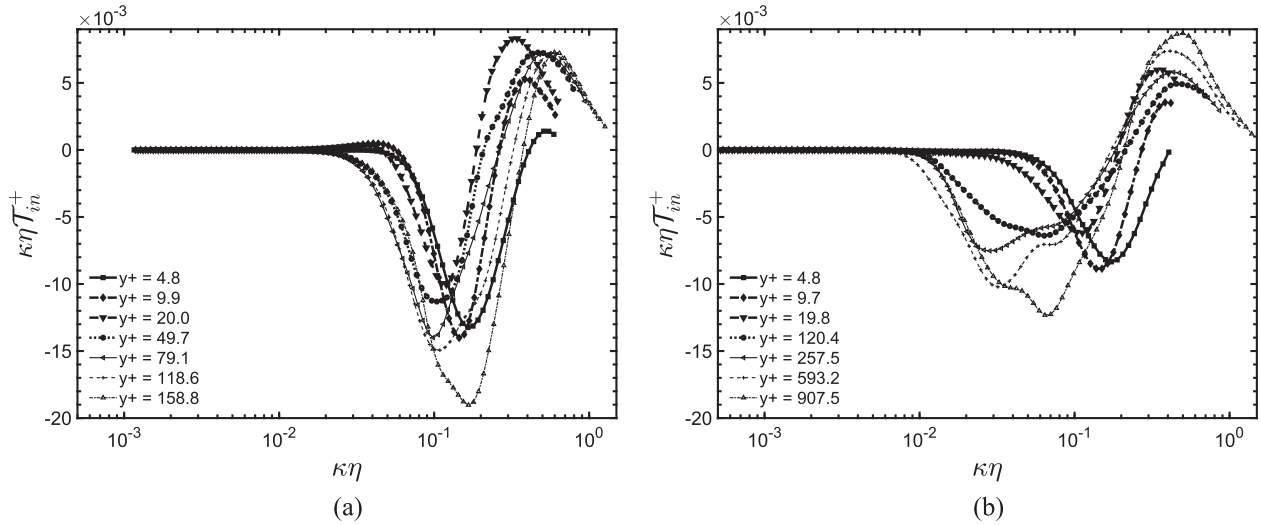

FIG. 14. In-plane non-linear transfer spectral density, $\kappa\eta\mathcal{T}^+_{in}$, at various y^+ locations at $Re_\tau = 180$ and 1000, respectively.

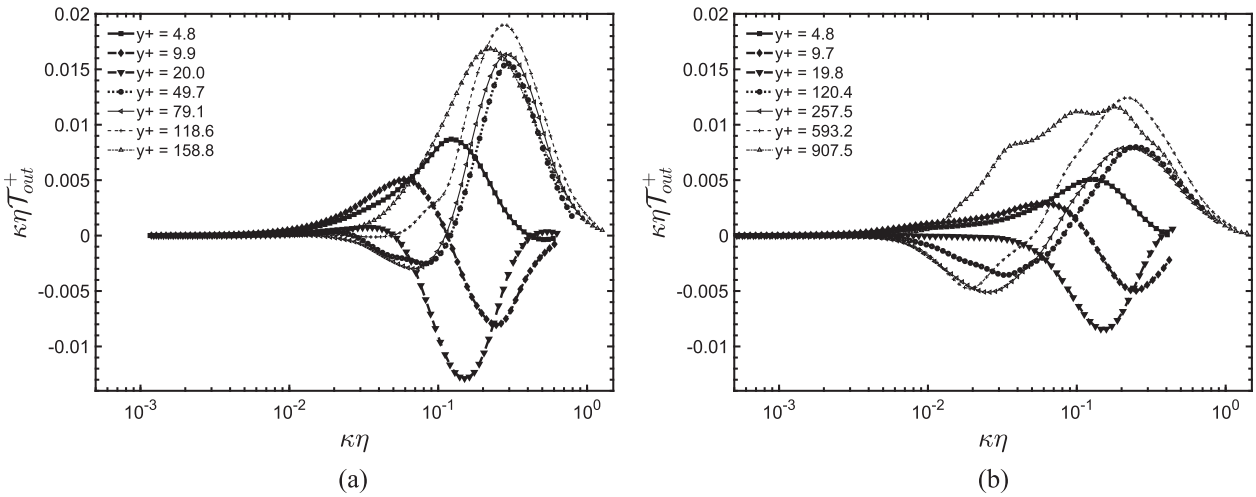

FIG. 15. Inter-plane non-linear transfer spectral density, $\kappa\eta\mathcal{T}^+_{out}$, at various y^+ locations at $Re_\tau = 180$ and 1000, respectively.

can be assessed. The inter-plane non-linear transfer term [Eq. (18)] is presented in Fig. 15. Both the inter- and in-plane non-linear turbulent transports have very little influence until $\kappa\eta \approx 2 \times 10^{-2}$ (cf. Figs. 14 and 15).

For both Reynolds numbers, the spectral distributions adjacent to the wall show that there is a transfer of energy into a broad range of scales. In addition, at $y^+ \approx 10$, an inverse energy cascade from intermediate to large spectral scales appears. In the buffer layer region $y^+ \approx 20$, the inter-plane non-linear transfer term acts to transfer energy out of these intermediate scales. Farther away from the wall, another inverse cascade appears, but with slightly different characteristics depending on Re_τ. At the lower Reynolds number, the intensity level of the energy transfer from the lower wavenumbers is less intense than the level of the increase of energy at the higher wavenumbers. At the higher Reynolds number, the difference in intensity levels is not as great and the energy transfer from the larger scales extends over a wider wavenumber range. As the mid-channel is approached, a net transfer of energy to a broad range of scales is found.

Similar to the spectral dissipation rate, the total non-linear transfer spectral density is composed of its in- and inter-plane contributions. When both results are combined, the total effect of the non-linear transfer term on the flow can be analyzed. The total non-linear term, $\mathcal{T}^+_{tot} = \mathcal{T}^+_{in} + \mathcal{T}^+_{out}$, is presented in Fig. 16. The inverse cascade energy flux is noticed in the near-to-wall region at both Reynolds numbers, for which, at the intermediate wavenumber range ($\kappa\eta \leq 0.1$), the total non-linear transfer acts as a source of energy, injecting energy coming from higher wavenumber. The inverse cascade comes from the combination of in- and inter-plane terms, for which, at $y^+ = 4.8$, $\kappa\eta\mathcal{T}_{in}$ acts as a sink of energy and $\kappa\eta\mathcal{T}_{out}$ acts as a source. In regions II–IV, the total non-linear transfer tends to transfer energy from larger to smaller scales.

Figure 17 shows the distribution of the viscous diffusion spectral density [Eq. (19)]. For $Re_\tau = 180$, adjacent to the wall and in the bulk flow, the diffusion spectral density acts primarily as a source of energy over a broad spectrum of scales. However, over the intermediate distances, the diffusion alternates between sink/source contributors covering

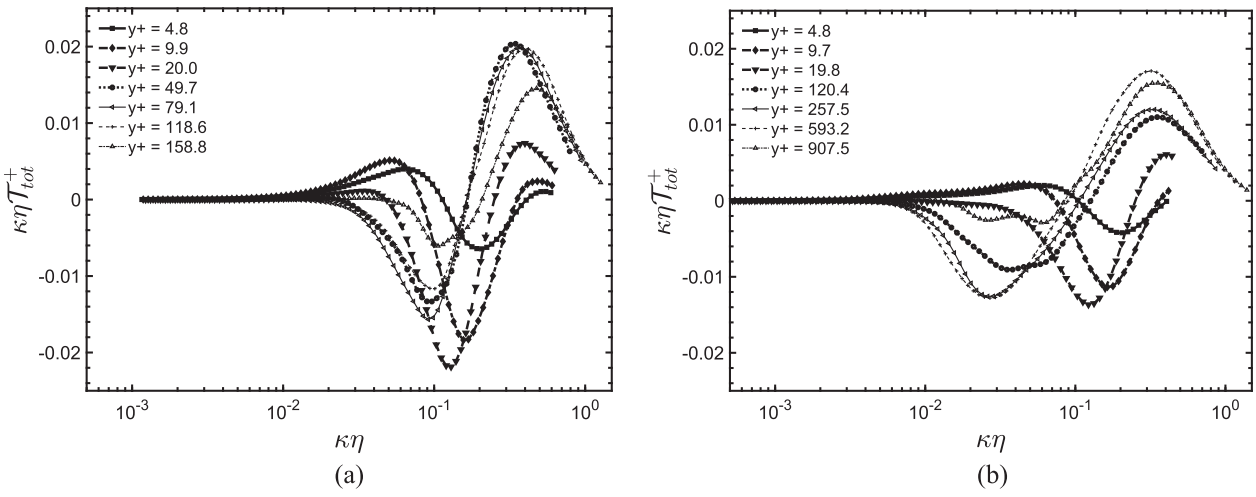

FIG. 16. Total non-linear transfer spectral density, $\kappa\eta\mathcal{T}^+_{tot}$, at various y^+ locations at $Re_\tau = 180$ and 1000, respectively.

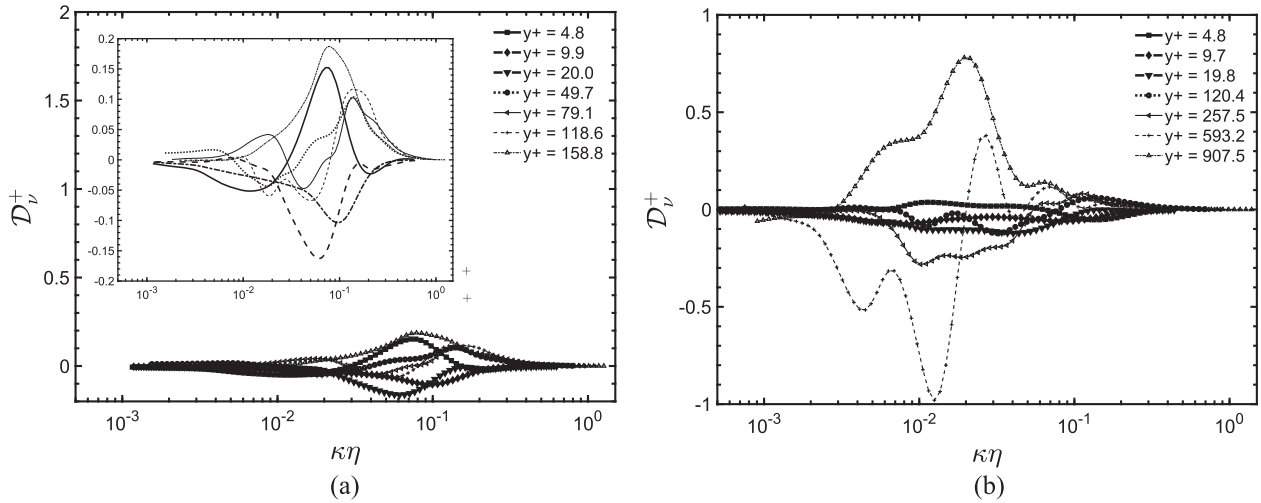

FIG. 17. Viscous diffusion spectral density, $\mathcal{D}_\nu^+$, at various y^+ locations at $Re_\tau = 180$ and 1000, respectively.

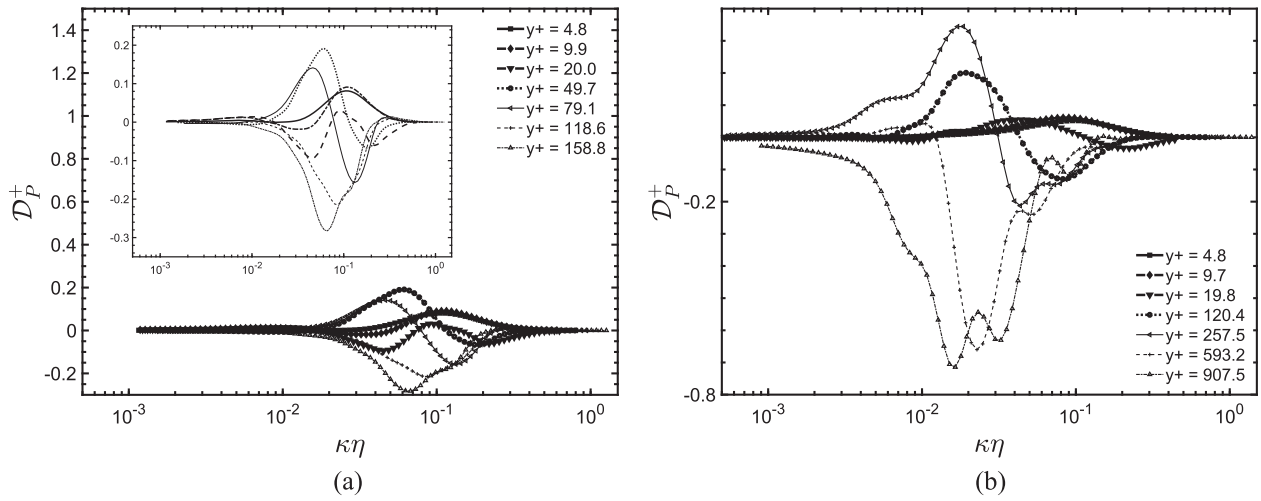

FIG. 18. Pressure diffusion spectral density, $\mathcal{D}_P^+$, at various y^+ locations at $Re_\tau = 180$ and 1000, respectively.

a broad spectrum of scales. For $Re_\tau = 1000$, the trends are less obvious. Adjacent to the wall and in the bulk region of the channel, the viscous spectral density acts as a source of energy over a broad spectrum of scales. Intermediate to these regions, the effect of the sink/source variations is less clear. These results are in contrast to the energy budget in physical space shown in Fig. 3, in which the contribution of the viscous diffusion across the channel is clear. This term is responsible for an energy exchange, where the energy is distributed practically to the whole wavenumber spectrum. Possibly, higher order reconstruction of the second derivative spectral function is required to develop a more precise representation of this term.

Figure 18 shows the pressure diffusion spectral density [Eq. (20)]. For $y^+ \leq 10$ in the lower Reynolds number flow, the pressure diffusion acts as an energy source, whereas, as the mid-channel is approached, the term acts as a sink across the affected scales. In the intermediate spatial flow regions, there are spectral oscillations resulting in sink and source contributions. At the higher Reynolds number, the behavior of the pressure diffusion as a source term for $y^+ \leq 10$ is similar to the low Reynolds number case. Additionally, in the bulk flow near the mid-channel, the effect reverses and the term acts as a sink. At intermediate distances from the wall, there is a migration from source to sink energy contribution with wall distance and also characterized by a spectral sink/source variation with wavenumber.

B. TKE budget in the spatial domain by wavenumber bands

In this section, we show the various source terms in Eq. (12) as a function of the wall distance, y^+, at several wavenumber bands, termed here bins. These terms are locally normalized according to Eq. (29). Following the approach by Bolotnov *et al.*,[2] the bin size and its distribution are shown in Fig. 19, for which the turbulent kinetic energy spectral density is illustrated at $y^+ \approx 40$. A total of 28 bins are defined, but for simplification, only 8 bins are plotted, which are highlighted in Figs. 20–27.

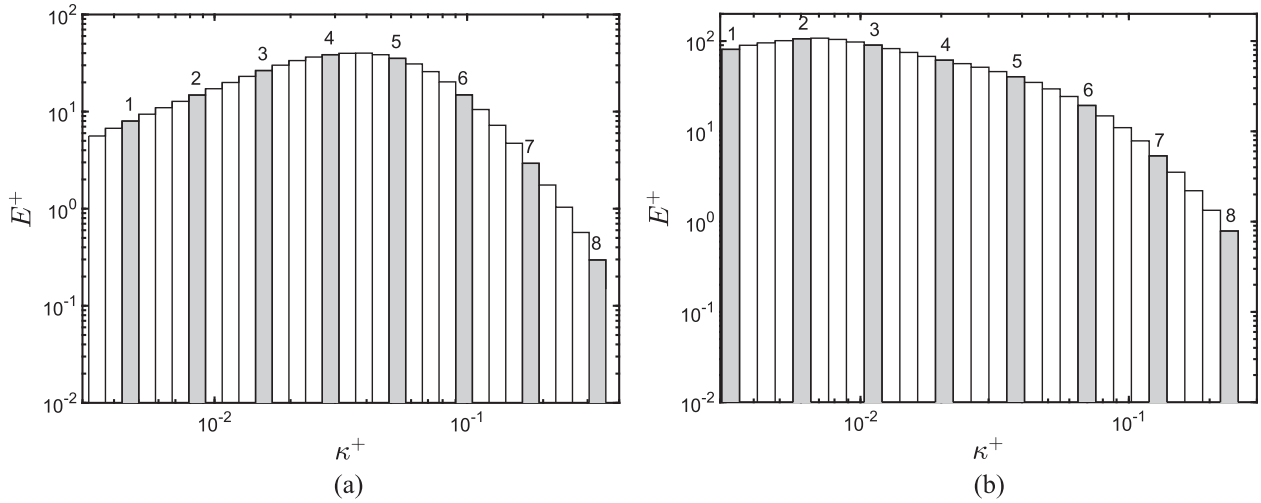

FIG. 19. Wavenumber bin distribution at $y^+ \approx 40$ and numeration plotted in Figs. 20–27 at $Re_\tau = 180$ and 1000, respectively.

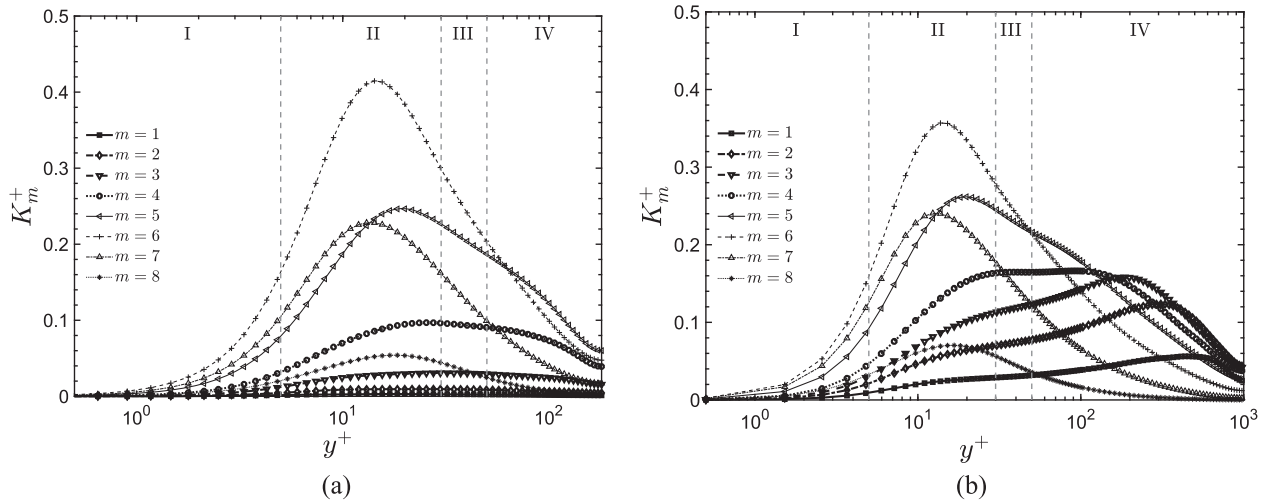

FIG. 20. Band distribution for turbulent kinetic energy of various wavenumber bins, K_m^+, vs. distance to the wall, y^+.

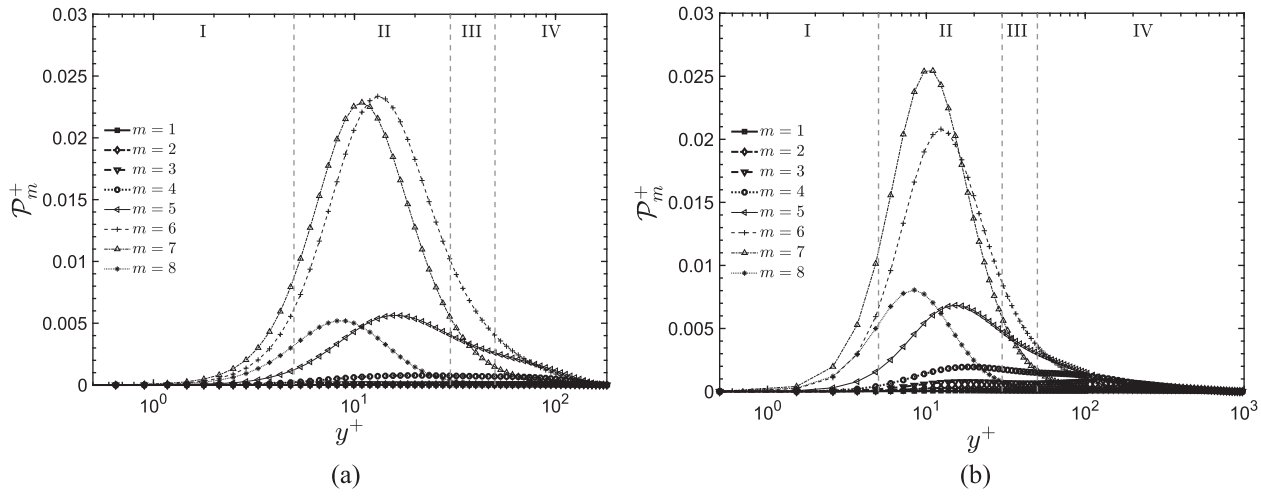

FIG. 21. Band distribution for turbulent production for various wavenumber bins, $\mathcal{P}_m^+$, vs. distance to the wall, y^+, at $Re_\tau = 180$ and 1000, respectively.

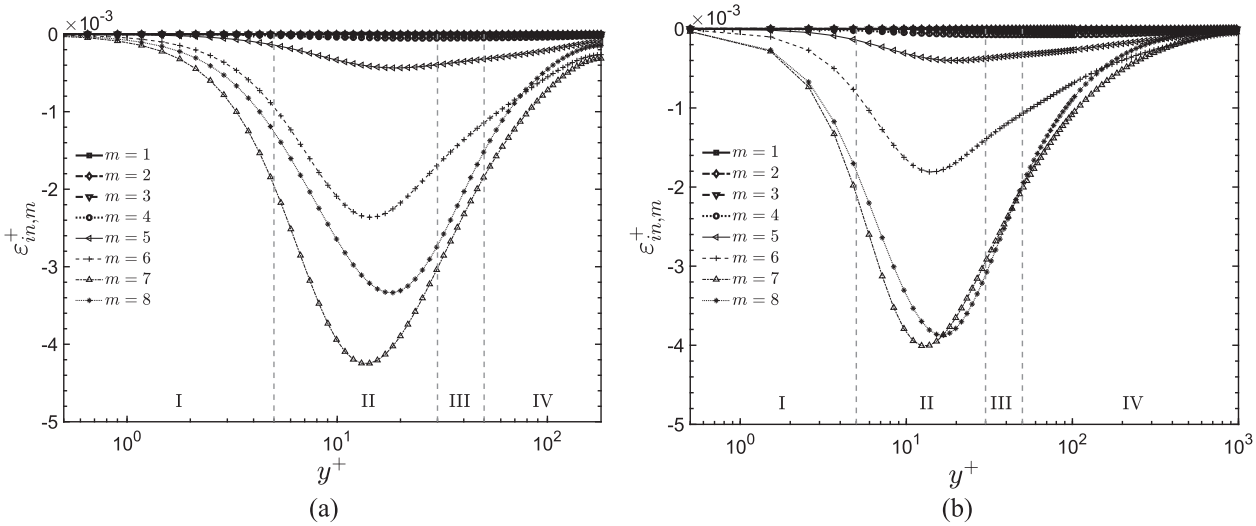

FIG. 22. Band distribution for in-plane turbulent dissipation for various wavenumber bins, $\varepsilon^+_{in,m}$, vs. distance to the wall, y^+, at $Re_\tau = 180$ and 1000, respectively.

Figure 20 shows the distribution of the turbulent kinetic energy. For both Reynolds numbers, the peaks of turbulent kinetic energy are located in the same region ($y^+ \approx 10$) and at the same spectral band (bin $m = 6$). For the $Re_\tau = 180$ flow, the energy bins $m = [1, 5]$ result in both an increase in turbulent kinetic energy and a shift in spatial location of peak energy within region II. Consistent with the trends shown in Fig. 19, bins $m = 6$ and 8 contribute decreasing amounts of energy with increasing wavenumber. At $Re_\tau = 1000$, the spectral contributions are complicated by the emergence of a second peak in energy input from bins $m = [1, 3]$ affecting the outer layer (region IV) of the channel. As Fig. 19 shows, these bins contain significant energy, although at lower wavenumbers (larger scales) than contributions relevant to the region of maximum turbulent kinetic energy (region II). Due to the broader inertial range shown for the high Reynolds number case in Fig. 19, bins $m = [4, 6]$ result in both the increase in energy in region II and the shift in the spatial location of peak turbulent energy. Energy input from bins $m = 7$ and 8 continues but at a lower level consistent with their spectral energy content.

The turbulent production contribution to the energy budget [Eq. (12)] is shown in Fig. 21. Although there is very little change in spatial distribution with the Reynolds number, a difference in energy content is found at the peak level of production. At the lower Reynolds number, there is an equal contribution from bins $m = 6$ and 7 to the energy production with the contribution from bin $m = 7$ (higher wavenumber band) resulting in a slight shift toward the wall in the peak production location. By contrast, at the higher Re_τ, the energy contribution from bin $m = 6$ is less intense than that from bin $m = 7$ with the peak production location remaining the same as in the lower Re_τ flow. Even though the energy content in the spectral band of bin $m = 7$ is larger for $Re_\tau = 180$ than $Re_\tau = 1000$, the peak of energy production is larger in the higher Reynolds number flow. Even in a higher Reynolds number, the peak of production is still located in the buffer layer,

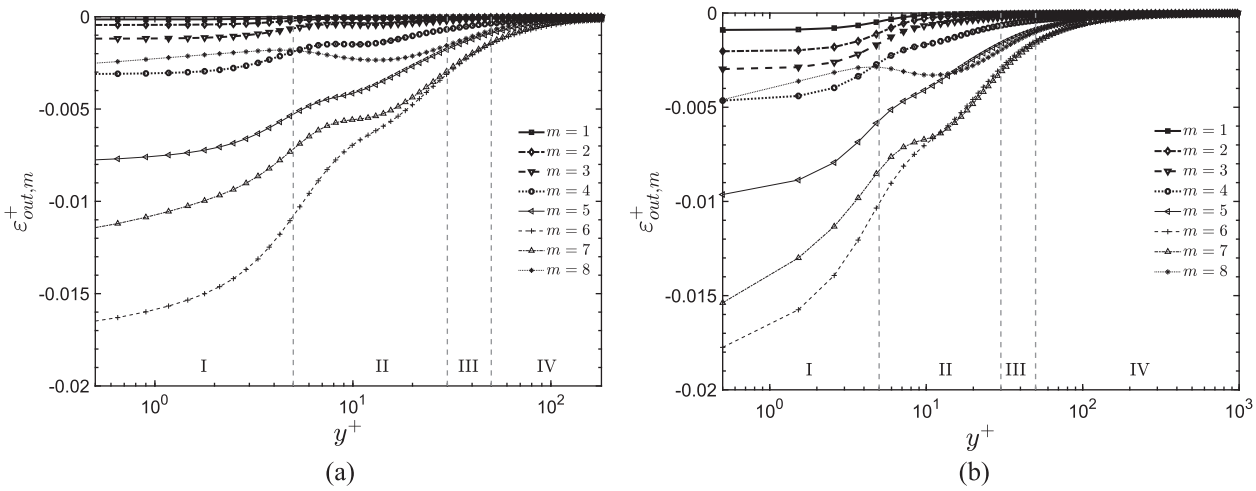

FIG. 23. Band distribution for inter-plane turbulent dissipation for various wavenumber bins, $\varepsilon^+_{out,m}$, vs. distance to the wall, y^+, at $Re_\tau = 180$ and 1000, respectively.

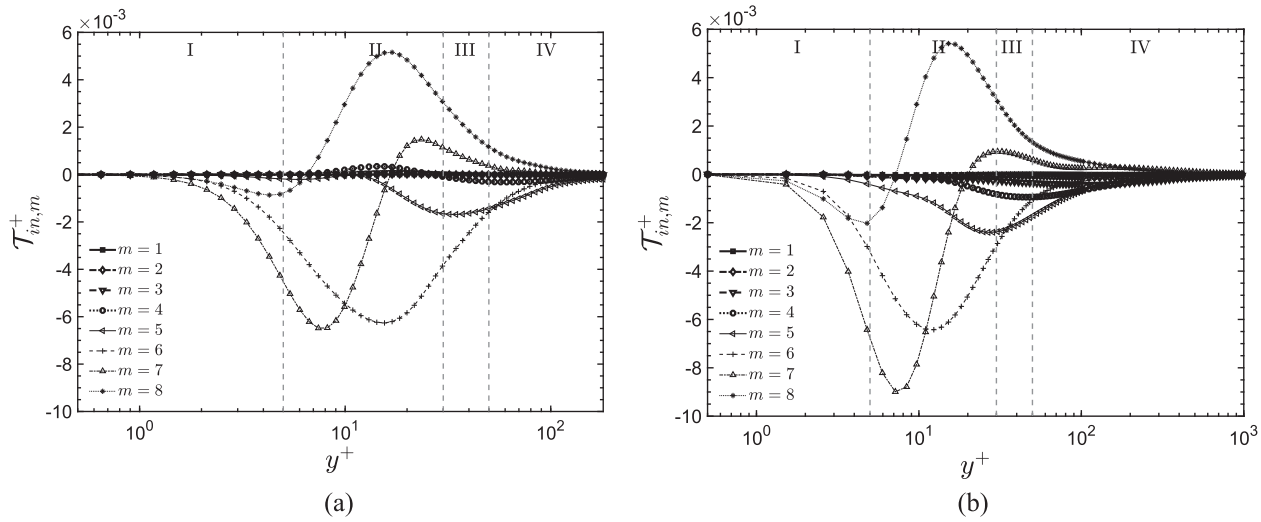

FIG. 24. Band distribution for in-plane non-linear transfer for various wavenumber bins, $\mathcal{T}^+_{in,m}$, vs. distance to the wall, y^+, at $Re_\tau = 180$ and 1000, respectively.

where TKE is created and then transferred to the center of the channel.

Figure 22 shows the in-plane turbulent dissipation band distribution. The most relevant spectral band contributions come from bins $m = [5, 8]$ and, once again, peak intensity values occur near $y^+ \approx 12$, consistent with the results in Figs. 15 and 16. The main difference between Reynolds number distributions lies in the relative contributions from bins $m = 7$ and 8. In the $Re_\tau = 180$ case, bin $m = 7$ is the primary contributor to peak dissipation intensity, whereas, for the $Re_\tau = 1000$ case, both bins $m = 7$ and 8 provide relatively equal contributions albeit at a slight shift in peak intensity location.

The remaining contribution to the energy dissipation is the inter-plane dissipation rate component. As shown in Fig. 23, this component acts as an overall drain of energy throughout primary regions I–III. Unlike the in-plane component, the inter-plane component is composed of spectral band contributions spanning all the selected bins. For both Reynolds numbers, there is a monotonic increase in inter-plane intensity distribution across the channel with increasing wavenumber band (bins $m = [1, 5]$). The largest contribution to the inter-plane intensity comes from bin $m = 6$, with subsequent higher wavenumber bins (bins $m = 7$ and 5). Since this term comes from the mean velocity gradients close to the wall, it shows decreasing intensity distributions across the channel, where the velocity gradient decreases. Unlike the in-plane distributions, whose maxima were in region II, all the maximum values in the inter-plane distributions occurred at the channel wall. The larger inter-plane intensity values relative to the in-plane contributions show that the spatial inhomogeneity in the wall-normal direction induces a much stronger energetic sink (across a broad spectrum of scales) than the in-plane spectral interaction.

The in-plane (Fig. 24) and inter-plane (Fig. 25), non-linear contributions are characterized by both a spectral band and a cross-channel energy transfer. For the in-plane non-linear transfer at $Re_\tau = 180$, low wavenumber energy bands (bins $m = [1, 3]$) make minimal contribution. Contributions from spectral bands bins $m = 4$, 5, and (primarily) 6 affect broad regions of the flow through large-to small-scale energy

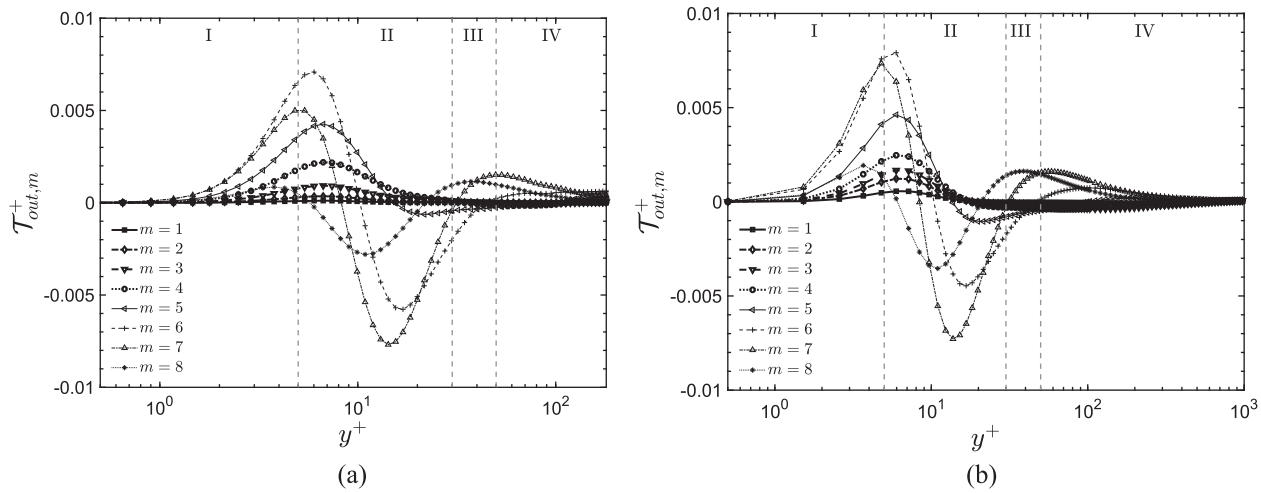

FIG. 25. Band distribution for inter-plane non-linear transfer for various wavenumber bins, $\mathcal{T}^+_{out,m}$, vs. distance to the wall, y^+, at $Re_\tau = 180$ and 1000, respectively.

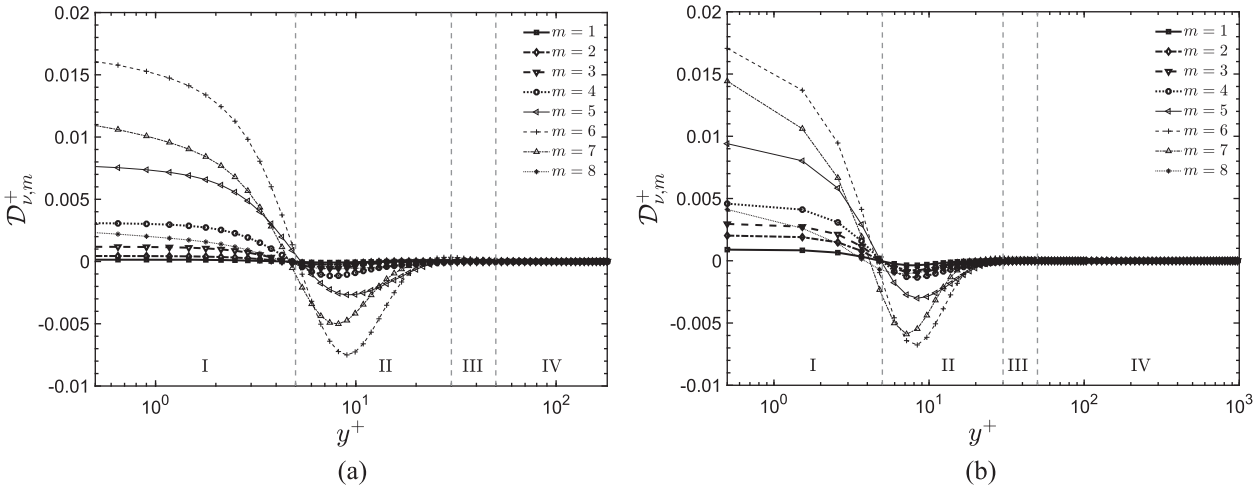

FIG. 26. Band distribution for turbulent viscous diffusion for various wavenumber bins, $\mathcal{D}^+_{\nu,m}$, vs. distance to the wall, y^+, at $Re_\tau = 180$ and 1000, respectively.

transfers acting as an overall sink in the energy budget. Across the buffer layer (region II), the contribution from the spectral band in bin $m = 7$ acts as both a sink and a source of energy. The crossover location appears to be above the production peak location at $y^+ \approx 16$. At the highest wavenumber band, bin $m = 8$, the non-linear term becomes an energy source over most of the outer layer, although, in a small spatial length in the lower buffer layer it acts as a sink. For the highest Reynolds number flow, $Re_\tau = 1000$, the qualitative features of the spectral distributions are similar; however, the lower wavenumber contributions from bins $m = 3$ and 4 become evident. Also, the higher wavenumber contributions from bins $m = [5, 8]$ penetrate closer to the wall and act as an energy sink to the smaller scale motions.

For the inter-plane non-linear transfer, Fig. 25, there is a spatial flux of energy toward the channel wall across a broad range of spectral scales (bins $m = [1, 4]$). For the higher spectral bands (bins $m = [5, 8]$), the spatial flux of energy shifts toward the bulk part of the flow. In addition to being dependent on the spectral band, this shift is also dependent on the distance from the wall. These qualitative features are similar for both Reynolds numbers, although differences in the magnitude and maximum intensity (spatial) location occur between $Re_\tau = 180$ and $Re_\tau = 1000$. The inter-plane non-linear transfer is responsible for an energy transfer from the buffer layer, where production holds its peak, adjacent regions. This energy flux results in an inverse cascade as noticed in Fig. 15.

The turbulent viscous diffusion contribution is shown in Fig. 26. Once again, there are little qualitative differences between Reynolds numbers. For both flows, the entire spectral band acts as a source of energy in region I and as a sink in region II, in other words, transferring energy from the buffer layer to the viscous sublayer. Quantitative differences in magnitude and maximum intensity location appear between flows, but each shows an intense source of energy near the wall with a weaker energy sink in the buffer layer. As it was noticed in Fig. 17, it may be noticed an inversion in the behavior of the viscous diffusion as it approaches the mid-channel region, switching from an energy source to a sink. This inversion is

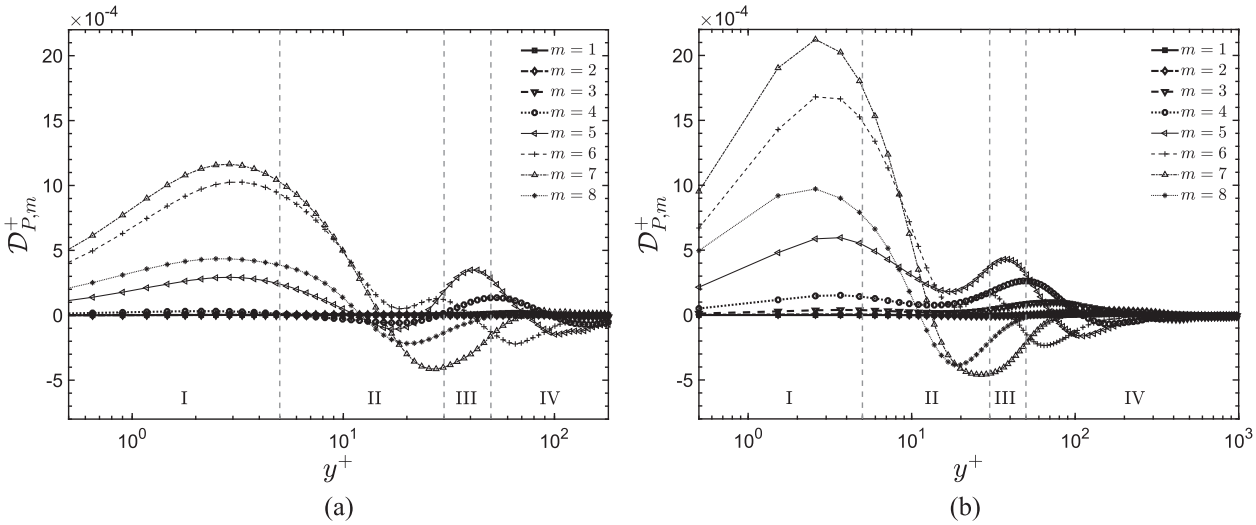

FIG. 27. Band distribution for pressure diffusion for various wavenumber bins, $\mathcal{D}^+_{P,m}$, vs. distance to the wall, y^+, at $Re_\tau = 180$ and 1000, respectively.

found to be closer to the wall at $Re_\tau = 1000$ than at $Re_\tau = 180$. This fact indicates that this term is responsible for an energy transfer in the physical domain rather than a scale-to-scale diffusion.

The pressure diffusion contribution is shown in Fig. 27. Although the pressure diffusion is small when compared to the other terms (see Fig. 3), it contributes to the energy transfer from the mid-channel region to the close-to-the-wall region, removing turbulent kinetic energy from the homogeneous and injecting in the inhomogeneous region. This transfer behavior occurs more significantly at larger wavenumbers (bins $m = [5, 8]$). At lower wavenumber (bins $m = [1, 4]$), since the average pressure term is homogeneous along the normal-to-wall direction, it presents a less pronounced dynamic to the spectral budget (see Fig. 18) and it becomes negligible. Two energy injection peaks are noticed, the higher one in the viscous sublayer (region I) and the second at the logarithmic layer (region III). In the center of the channel, the transfer is negligible. The Reynolds number influence on the pressure diffusion occurs mainly in the close-to-wall region (region I), with an increasing peak intensity when the Reynolds number is increased.

V. SUMMARY

The analysis of the dynamics of fully developed turbulent flows in channels has long been the subject of study, initially through physical experiments to ensure sufficiently high Reynolds numbers reflective of engineering relevant flows and more recently through numerical simulations to facilitate the detailed analysis of the underlying energetic dynamics. The inherent coupling between the inhomogeneity of the turbulence in the direction of mean shear and the homogeneity in planes perpendicular to the shear readily lends itself to an analysis of some basic underlying characteristic features of the turbulence itself, that is, homogeneity, inhomogeneity, and anisotropy.

The results from the numerical simulations of turbulent channel flows have been important contributors to the development and validation of Reynolds-averaged model prediction tools through the analysis of single-point velocity (and/or scalar flux) correlations. More recently, analyses have been extended to two-point velocity correlations and structure functions using mathematical formalisms originating with Kolmogorov[17] and further exploited since Refs. 5, 18, and 21. From numerical results at low Reynolds numbers, the physical space structure function correlations have been used to develop a detailed picture of the dynamic exchange among energetic scales of motion. However, single-point analyses were important to the successful development of the Reynolds-Averaged Navier-Stokes (RANS) prediction tools, such structure function studies also have relevance to the sub-grid scale (SGS) modeling required for large eddy simulation, hybrid RANS/LES methods, and other multi-scale methods.

In this study, a fully spectral approach has been followed that isolates the effect of the mean shear inhomogeneity and the planar homogeneity characteristic of the fully developed channel flow as well as offering a comparative analysis of results at $Re_\tau = 180$ and $Re_\tau = 1000$, respectively. A validation of the methodology has also been performed with a comparison with results from a previous study[2] at a low Reynolds number. The transport equation for the energy spectral density has been derived and partitioned into terms representing the in-plane (homogeneous direction) and inter-plane (inhomogeneous direction) energetic transfer. The energetic scale transfer has been analyzed as a function of wavenumber at various locations across the channel. The results showed that the spectral range of the relevant energetic dynamics for the $Re_\tau = 180$ case was narrower than the corresponding range for the $Re_\tau = 1000$ case. Among the results, a spectral broadening at the higher Reynolds number due to an increase in the lower wavenumber scales was shown. This increase was found to primarily affect the bulk region of the flow for the majority of energetic budget terms. Also presented was an analysis of the energetic scale transfer as a function of wall distance at different wavenumber bands. These results showed that the primary contributions to the energetic dynamics across the channel were due to spectral scales in the inertial range and higher. Near the wall, the spectral content of the budget terms varied little between Reynolds numbers. Away from the wall, in the buffer layer and into the bulk layer, more variation in energy band contributions was found.

In addition to the insights into the energetic dynamics provided by this spectral budget study, the results obtained here are relevant to the improved development of SGS models for use in multi-scale methods including both LES and hybrid RANS/LES. Demands on multi-scale methods, such as LES and hybrid RANS-LES, to yield flow field solutions to ever increasing complex flows are increasing. While increased temporal and spatial resolution will inherently improve the solution accuracy, the associated increased costs severely curtail the feasibility of using such methodologies. As with all turbulent solution methodologies requiring some form of modeling, it is the quality of the models to accurately replicate the effects of the unresolved motions that correlate with the overall flow field solution. For LES and hybrid methods, this means that the effects of the unresolved and/or subfilter scale motions need to be accurately replicated. It has long been known that the backscatter[24] plays a pivotal role in the energetic dynamics. A detailed knowledge of the influence of inhomogeneity and anisotropy as well as the influence of the Reynolds number on the spectral behavior can significantly improve the predictability of the functional modeling of the subgrid and subfilter scales (see Ref. 29). For instance, Chaouat and Schiestel,[3] by using the spectral transfer concept, proposed a new large eddy simulation model, where the energy transfers for the subgrid turbulent TKE were tracked. Cimarelli and De Angelis[4] studied how a new subgrid-scale modeling approach could be enhanced by new physical concepts based on the multi-dimensional feature of energy transfer. On the side of RANS models, DNS is able to provide very detailed data in order to estimate the quality of different turbulence modeling approaches. For instance, as pointed out by Bolotnov *et al.*,[1] the understanding of the spectral and spatial turbulent kinetic energy transfer can help the modeling of the energy transfers between liquid eddies of different sizes and the energy exchanges between dispersed bubbles and liquid eddies.

Increasing computational capabilities (speed/memory) are motivating factors in the improvement of numerical resolution and the ability to compute increasingly higher Reynolds number flows. Although the focus here has been on the velocity correlations and the corresponding spectral field, similar analyses can be conducted for turbulent scalar flux correlations or more complex fluids, such as generalized-Newtonian and viscoelastic fluids. In these cases, the fluid imparts onto the turbulent flow an additional contributor to compose the energetic dynamic balance.

ACKNOWLEDGMENTS

This research has granted access to the HPC resources of CCRT/CINES/IDRIS under the allocation i20162b2277 made by GENCI (Grand Equipement National de Calcul Intensif). The data used herein were produced on the IBM Blue Gene/Q computer Turing at the IDRIS/CNRS computing center, Orsay, France. Local support from the Centre de Ressources Informatiques (CRI) of the University of Lille has been very useful for post-processing and is also acknowledged.

The authors also would like to acknowledge the financial technical support from the Petróleo Brasileiro S.A. (Petrobras), the Brazilian funding agencies Coordenadoria de Aperfeiçoamento de Pessoal de Nível Superior (CAPES), and Conselho Nacional de Desenvolvimento Científico e Tecnológico (CNPq) by means of the program "Science without Boarders."

APPENDIX: RESULTS VALIDATION

In this section, the validation of the energy transfer at $Re_\tau = 180$ is presented. Validation is made by comparing the results of the present paper with data from the study by Bolotnov *et al.*[2] ($Re_\tau = 178.12$). Figure 28 shows the comparison between the bin distributions and numerations used in the present study and the study by Bolotnov *et al.*[2] The bin structure in the present study seeks to be similar to the previous study by Bolotnov *et al.*[2] in order to facilitate and enable comparative analyses between this and the previous work.

Figures 29–32 show the comparison between the contour levels of turbulent kinetic energy, turbulent production, and

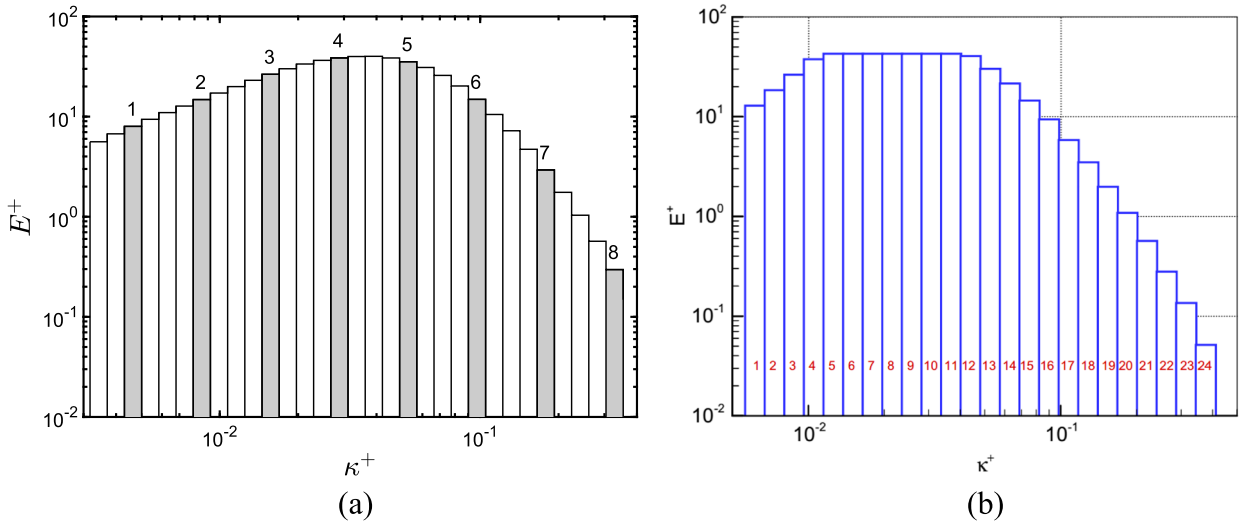

FIG. 28. Comparison of the wavenumber bin distribution and numeration between the present paper and the one by Bolotnov *et al.*[2]

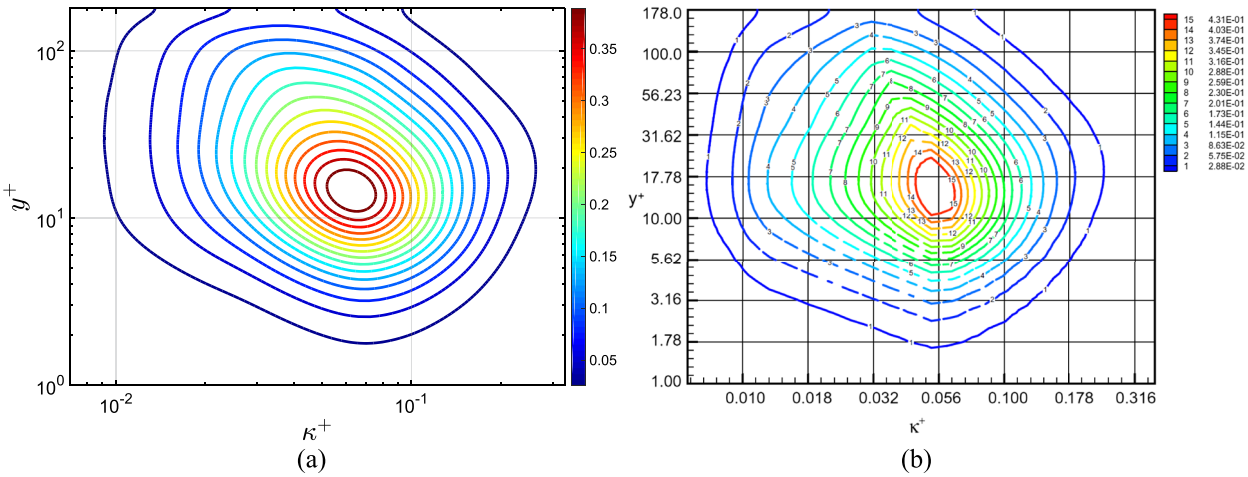

FIG. 29. Comparison of turbulent kinetic energy contour levels at $Re_\tau = 180$ between the present work and the study by Bolotnov *et al.*,[2] respectively.

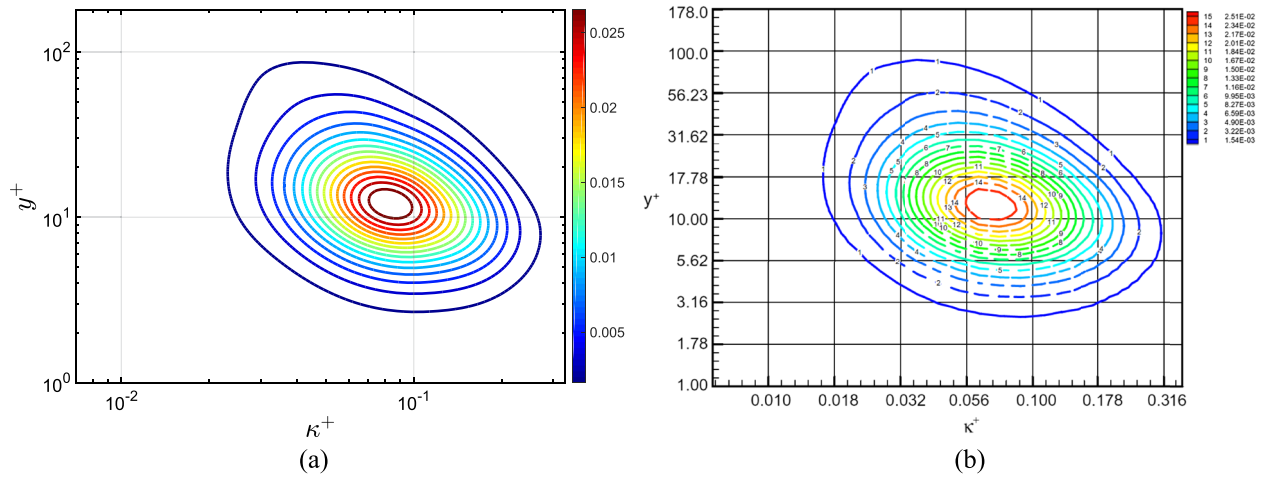

(a) (b)

FIG. 30. Comparison of turbulent production contour levels at $Re_\tau = 180$ between the present work and the study by Bolotnov *et al.*,[2] respectively.

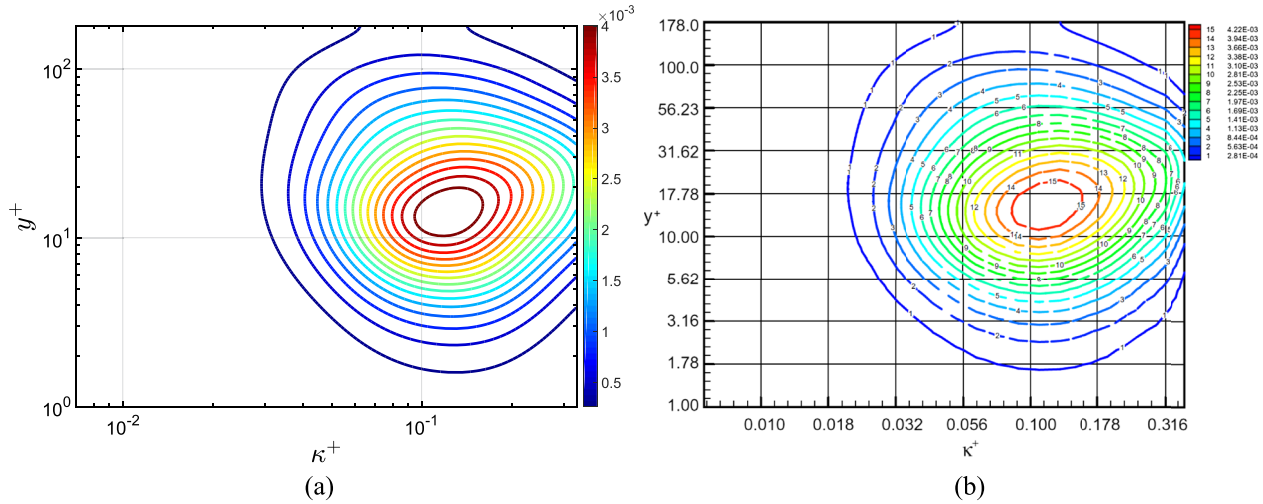

(a) (b)

FIG. 31. Comparison of in-plane turbulent dissipation contour levels at $Re_\tau = 180$ between the present work and the study by Bolotnov *et al.*,[2] respectively.

in-plane and inter-plane turbulent dissipation rate, respectively. These comparisons show that the current results match with those of Bolotnov *et al.* in terms of magnitude and global shape.[2]

Figures 33–39 show the comparison of the various source terms from Eq. (12) integrated in bin regions as a function of wall distance y^+ at several wavenumber bins [the normalization used is given in Eq. (29)].

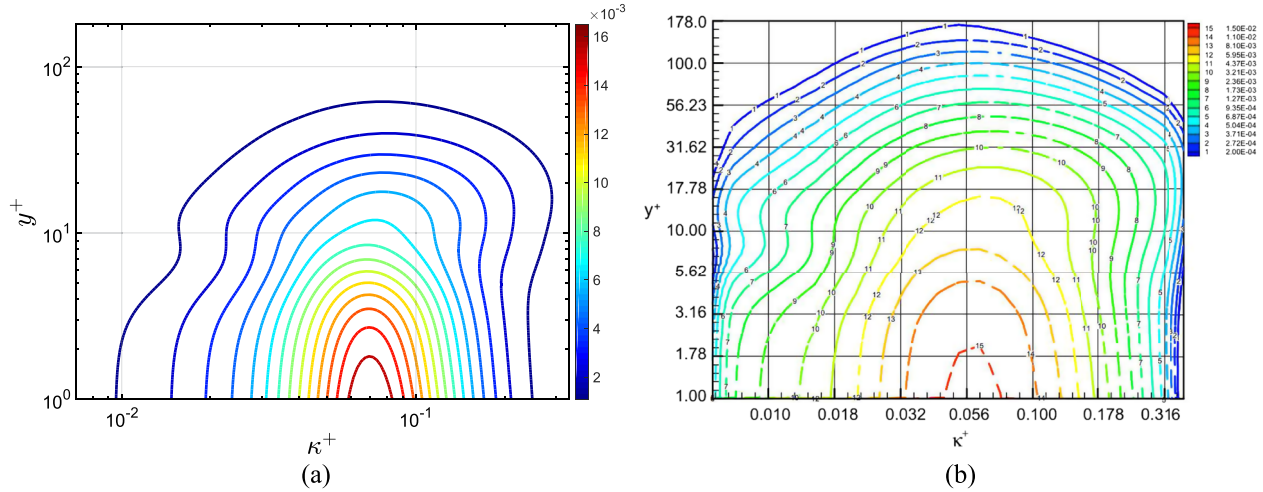

(a) (b)

FIG. 32. Comparison of inter-plane turbulent dissipation contour levels at $Re_\tau = 180$ between the present work and the study by Bolotnov *et al.*,[2] respectively.

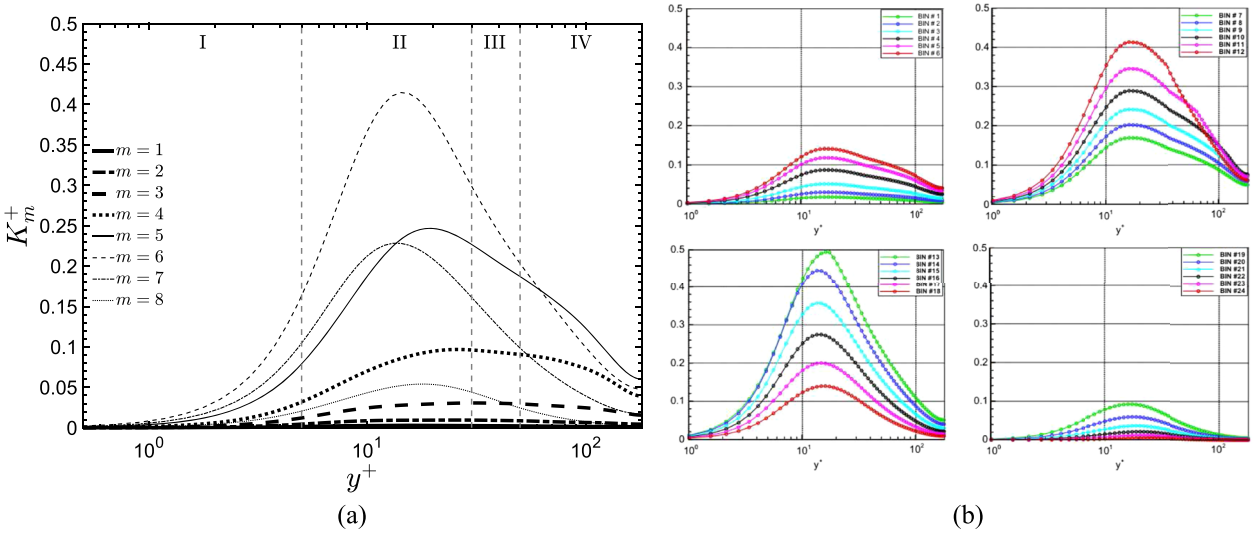

FIG. 33. Band distribution of turbulent kinetic energy of various wavenumber bins, K_m^+, vs. distance to the wall between the present work and the study by Bolotnov *et al.*,[2] respectively.

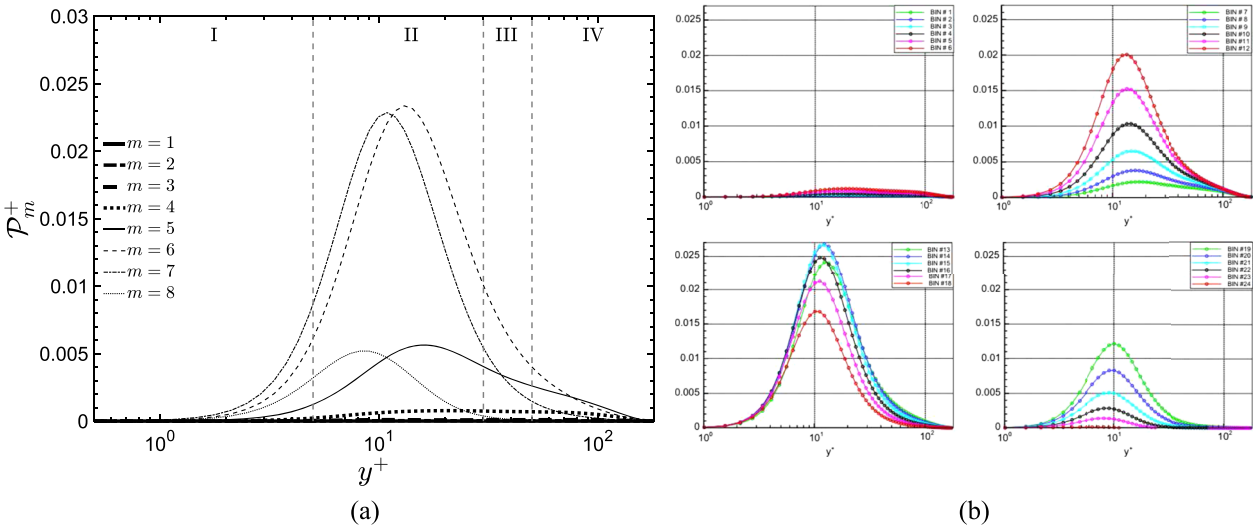

FIG. 34. Turbulent production spectral band distribution vs. distance to the wall between the present work and the study by Bolotnov *et al.*,[2] respectively.

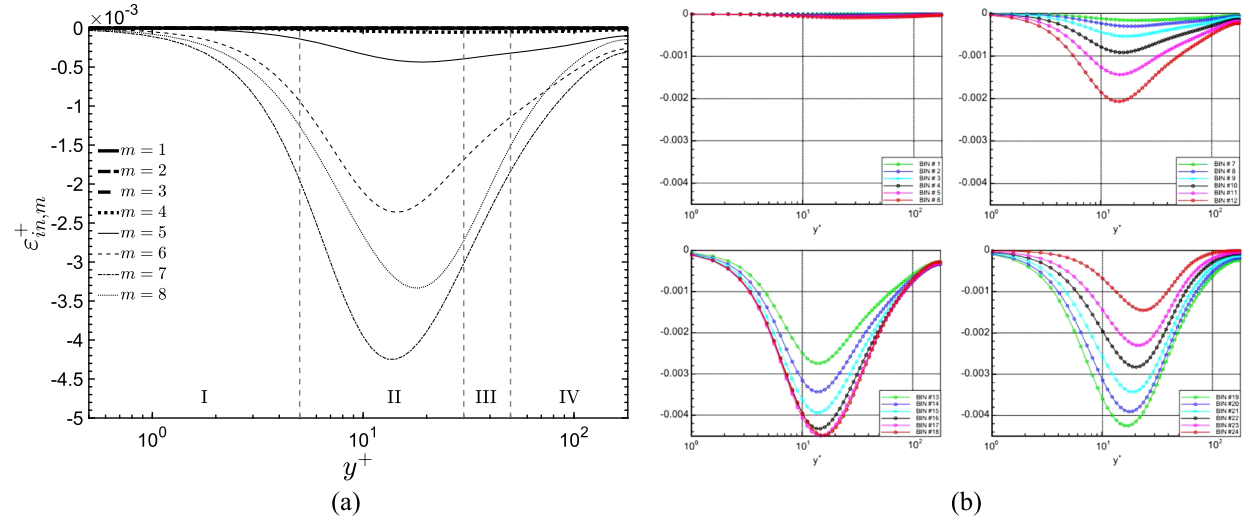

FIG. 35. In-plane turbulent dissipation spectral band distribution vs. distance to the wall between the present work and the study by Bolotnov *et al.*,[2] respectively.

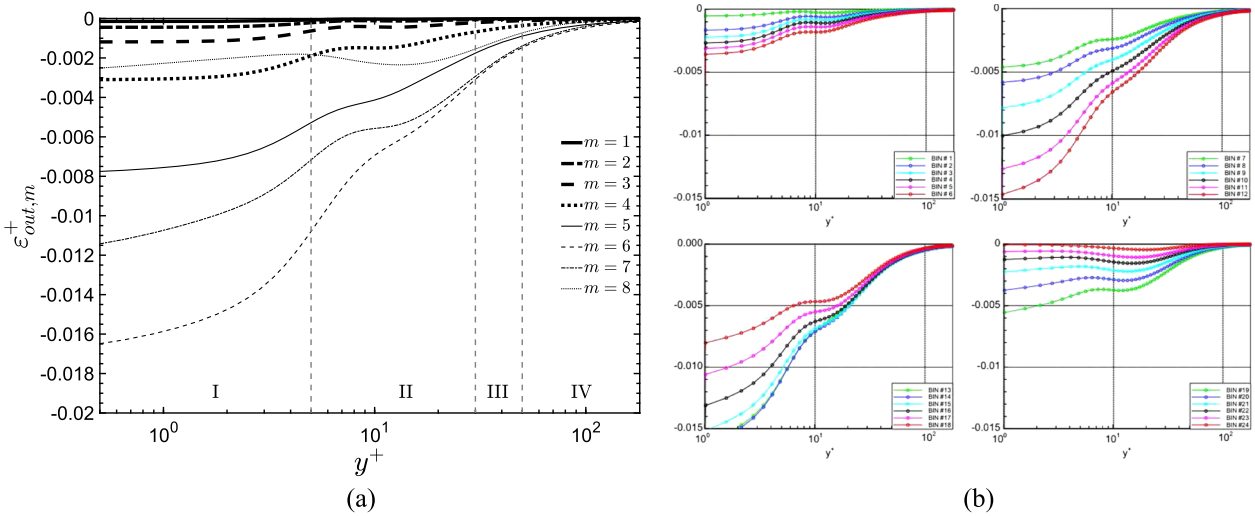

FIG. 36. Inter-plane turbulent dissipation spectral band distribution vs. distance to the wall between the present work and the study by Bolotnov *et al.*,[2] respectively.

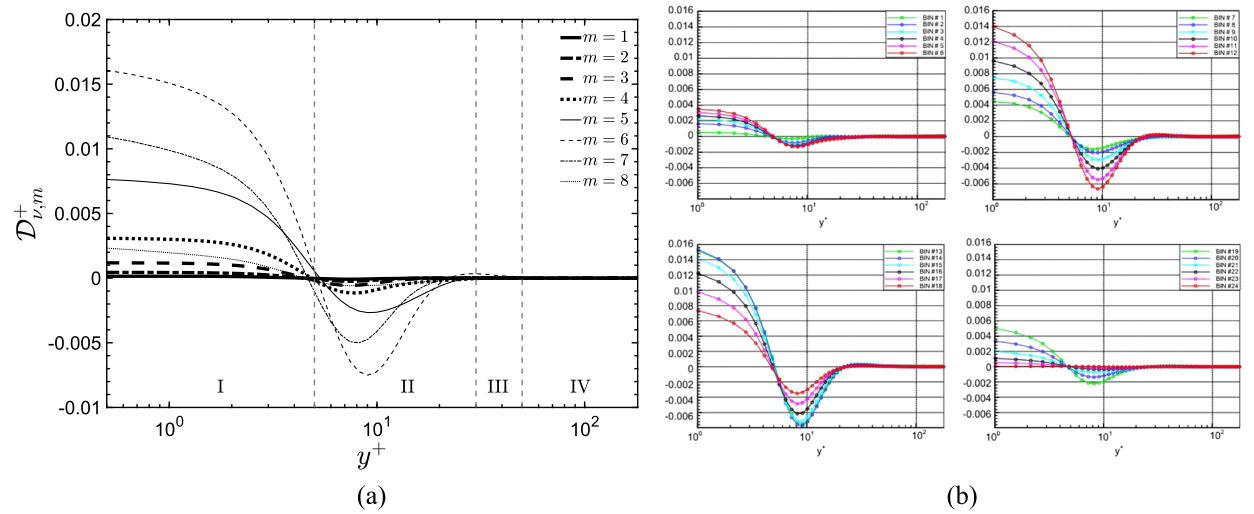

FIG. 37. Turbulent viscous diffusion spectral band distribution vs. distance to the wall between the present work and the study by Bolotnov *et al.*,[2] respectively.

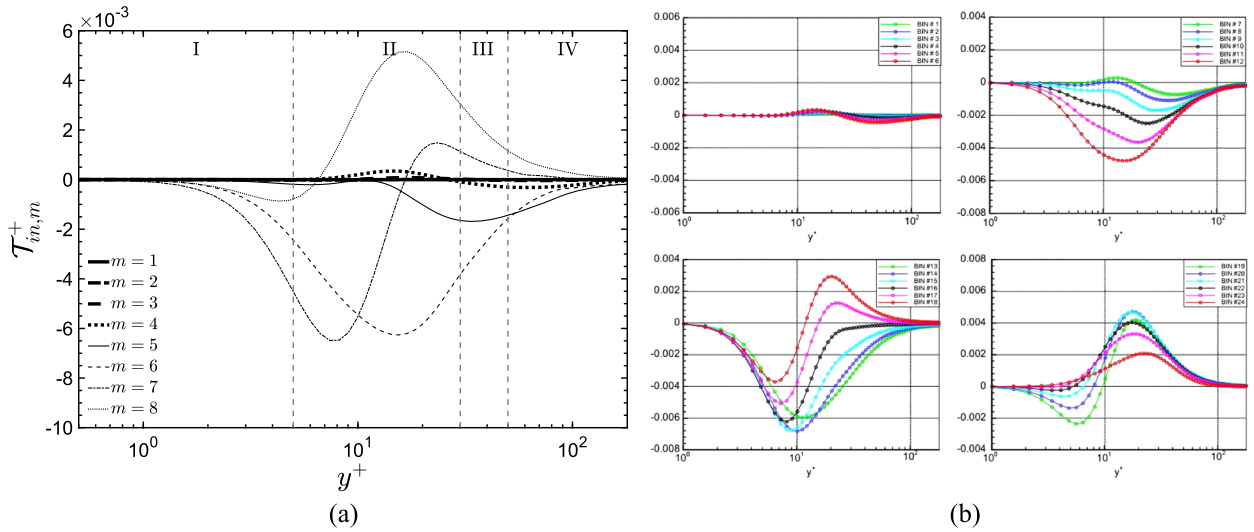

FIG. 38. In-plane non-linear transfer term spectral band distribution vs. distance to the wall between the present work and the study by Bolotnov *et al.*,[2] respectively.

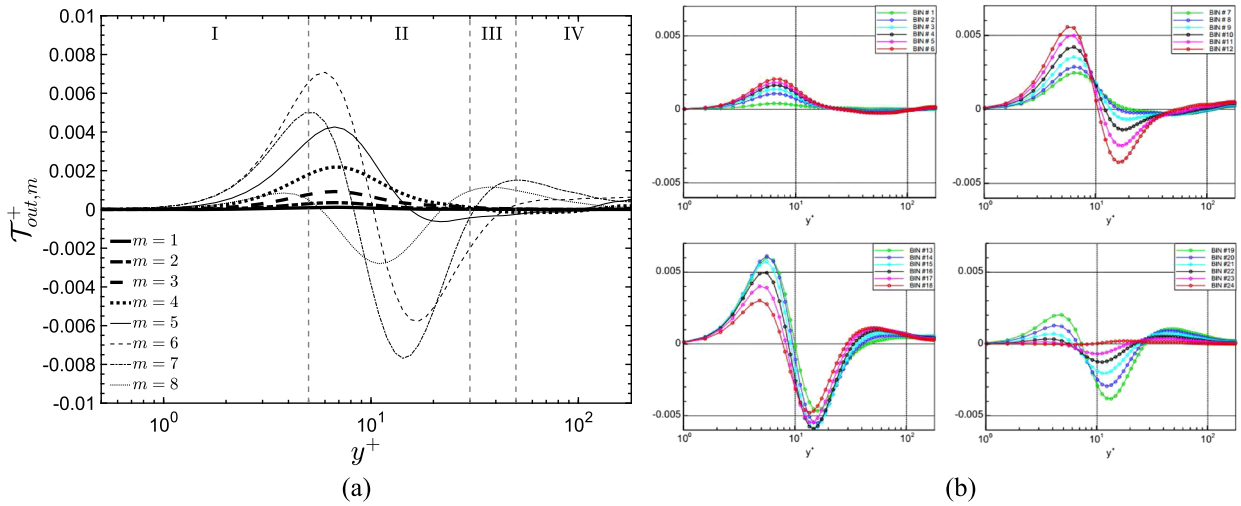

FIG. 39. Inter-plane non-linear transfer term spectral band distribution vs. distance to the wall between the present work and the study by Bolotnov *et al.*,[2] respectively.

The present results have been found to be in good agreement with those of the study by Bolotnov *et al.*[2] The qualitative comparison presented in Figs. 29–32 reveals that the shapes of the energy distribution match with those of Bolotnov *et al.*[2] with respect to the source and sink peak positions. Besides that, the global shapes are similar. The only exception is the inter-plane dissipation (Fig. 32), for which even if the peaks are in the same location and have similar magnitude, there is a slight difference in the energy distribution at small κ^+ and in the center of the channel.

For the quantitative results showing the behavior of the spectral band energy distribution of each term for different bins depending on the distance to the wall (Figs. 33–39), it can be noticed that the present results are consistent with those of Bolotnov *et al.*[2] with respect to peak locations and magnitudes. The behavior of each source term varying with y^+ also corroborates the results of Bolotnov *et al.*[2]

[1] Bolotnov, Jr., I. A., Lahey, R. T., Drew, D. A., and Jansen, K. E., "Turbulent cascade modeling of single and bubbly two-phase turbulent flows," Int. J. Multiphase Flow **34**, 1142–1151 (2008).

[2] Bolotnov, I. A., Lahey, Jr., R. T., Drew, D. A., Jansen, K. E., and Oberai, A. A., "Spectral analysis of turbulence based on the DNS of a channel flow," Comput. Fluids, **39**(4), 640–655 (2010).

[3] Chaouat, B. and Schiestel, R., "A new partially integrated transport model for subgrid-scale stresses and dissipation rate for turbulent developing flows," Phys. Fluids **17**, 065106 (2005).

[4] Cimarelli, A. and De Angelis, E., "The physics of energy transfer toward improved subgrid-scale models," Phys. Fluids **26**(5), 055103 (2014).

[5] Cimarelli, A., De Angelis, E., and Casciola, C., "Paths of energy in turbulent channel flows," J. Fluid Mech. **715**, 436–451 (2013).

[6] Comte-Bellot, G. and Corrsin, S., "The use of a contraction to improve the isotropy of grid-generated turbulence," J. Fluid Mech. **25**, 657 (1966).

[7] Del Álamo, J. C. and Jiménez, J., "Spectra of the very large anisotropic scales in turbulent channels," Phys. Fluids **15**(6), L41 (2003).

[8] Del Álamo, J. C., Jiménez, J., Zandonade, P., and Moser, R. D., "Scaling of the energy spectra of turbulent channels," J. Fluid Mech. **500**, 135–144 (2004).

[9] Domaradzki, J. A. and Rogallo, R. S., "Local energy transfer and nonlocal interactions in homogeneous, isotropic turbulence," Phys. Fluids **2**(3), 413–426 (1990).

[10] Dunn, D. C. and Morrison, J. F., "Analysis of the energy budget in turbulent channel flow using orthogonal wavelets," Comput. Fluids **34**, 199 (2005).

[11] George, W. K., "The decay of homogeneous isotropic turbulence," Phys. Fluids A **4**, 1492 (1992).

[12] Gualtieri, P., Casciola, C. M., Benzi, R., and Piva, R., "Preservation of statistical properties in large-eddy simulation of shear turbulence," J. Fluid Mech. **592**, 471–494 (2007).

[13] Hill, R. J., "Equations relating structure functions of all orders," J. Fluid Mech. **434**, 379–388 (2001).

[14] Hill, R. J., "Exact second-order structure-function relationship," J. Fluid Mech. **468**, 317–326 (2002).

[15] Hoyas, S. and Jiménez, J., "Scaling of the velocity fluctuations in turbulent channels up to $Re_\tau = 2003$," Phys. Fluids **18**(1), 011702 (2006).

[16] Jiménez, J., "The physics of wall turbulence," Phys. A **263**, 252–262 (1999).

[17] Kolmogorov, A., "The local structure of turbulence in incompressible viscous fluid for very large Reynolds numbers," Dokl. Akad. Nauk SSSR **30**(1890), 301–305 (1941).

[18] Marati, N., Casciola, C., and Piva, R., "Energy cascade and spatial fluxes in wall turbulence," J. Fluid Mech. **521**, 191–215 (2004).

[19] Moin, P. and Mahesh, K., "Direct numerical simulation: A tool in turbulent research," Annu. Rev. Fluid Mech. **30**, 539–578 (1998).

[20] Mollicone, J.-P., Battista, F., Gualtieri, P., and Casciola, C. M., "Effect of geometry and Reynolds number on the turbulent separated flow behind a bulge in a channel," J. Fluid Mech. **823**, 100–133 (2017).

[21] Mollicone, J.-P., Battista, F., Gualtieri, P., and Casciola, C. M., "Turbulence dynamics in separated flows: The generalised Kolmogorov equation for inhomogeneous anisotropic conditions," J. Fluid Mech. **841**, 1012–1039 (2018).

[22] Moser, R. D., Kim, J., and Mansour, N. N., "Direct numerical simulation of turbulent channel flow up to $Re_\tau = 590$," Phys. Fluids **11**, 943–945 (1999).

[23] Oliver, T. A., Malaya, N., Ulerich, R., and Moser, R. D., "Estimating uncertainties in statistical category computed from direct numerical simulation," Phys. Fluids **26**, 035101 (2014).

[24] Piomelli, U., Cabot, W. H., Moin, P., and Lee, S., "Subgrid-scale backscatter in turbulent and transitional flows," Phys. Fluids A **3**(7), 1766 (1991).

[25] Piomelli, U., Yu, Y., and Adrian, R. J., "Subgrid-scale energy transfer and near-wall turbulence structure," Phys. Fluids **8**, 215 (1996).

[26] Pope, S. B., "A more general effective-viscosity hypothesis," J. Fluid Mech. **72**, 331–334 (1975).

[27] Pope, S. B., *Turbulent Flows* (Cambridge University Press, 2000).

[28] Richardson, L. F., *Weather Prediction by Numerical Process* (Cambridge University Press, 1922).

[29] Sagaut, P., in *Large Eddy Simulation for Incompressible Flows: An Introduction*, Scientific Computation, edited by Sagaut, P. and Meneveau, C. (Amazon.com: Books, 2005), ISBN: 9783540263449.

[30] Schiavo, L. A. C. A., Wolf, W. R., and Azevedo, J. L. F., "Turbulent kinetic energy budgets in wall bounded flows with pressure gradients and separation," Phys. Fluids **29**(11), 115108 (2017).

[31] Skrbek, L. and Stalp, S. R., "On the decay of homogeneous isotropic turbulence," Phys. Fluids **12**, 1997 (2000).

[32]Tennekes, H. and Lumley, J. L., *A First Course in Turbulence* (The MIT Press, Cambridge, Massachusetts, London, England, 1972).
[33]Thais, L., Tejada-Martnez, A. E., Gatski, T. B., and Mompean, G., "A massively parallel hybrid scheme for direct numerical simulation of turbulent viscoelastic channel flow," Comput. Fluids **43**(1), 134–142 (2011).
[34]Thais, L., Mompean, G., and Gatski, T. B., "Spectral analysis of turbulent viscoelastic and Newtonian channel flows," J. Non-Newtonian Fluid Mech. **200**, 165–176 (2013).
[35]Trofimova, A., Tejada-Martinez, A. E., Jansen, K. E., and Lahey, Jr., R. T., "Direct numerical simulation of turbulent channel flows using a stabilized finite element method," Comput. Fluids, **38**(4), 924–938 (2009).
[36]Zhou, Y., "Degrees of locality of energy transfer in the inertial range," Phys. Fluids **5**(5), 1092–1094 (1993a).
[37]Zhou, Y., "Interacting scales and energy transfer in isotropic turbulence," Phys. Fluids **5**(10), 2511–2524 (1993b).